# Multiplex, quantitative cellular analysis in large tissue volumes with clearing-enhanced 3D microscopy ($C_e$3D)

Weizhe Li[a], Ronald N. Germain[a,1], and Michael Y. Gerner[a,b,1]

[a]Lymphocyte Biology Section, Laboratory of Systems Biology, National Institute of Allergy and Infectious Diseases/NIH, Bethesda, MD 20892; and [b]Department of Immunology, University of Washington, Seattle, WA 98109

Contributed by Ronald N. Germain, July 19, 2017 (sent for review May 31, 2017; reviewed by Marc K. Jenkins and Mark J. Miller)

**Organ homeostasis, cellular differentiation, signal relay, and in situ function all depend on the spatial organization of cells in complex tissues. For this reason, comprehensive, high-resolution mapping of cell positioning, phenotypic identity, and functional state in the context of macroscale tissue structure is critical to a deeper understanding of diverse biological processes. Here we report an easy to use method, clearing-enhanced 3D ($C_e$3D), which generates excellent tissue transparency for most organs, preserves cellular morphology and protein fluorescence, and is robustly compatible with antibody-based immunolabeling. This enhanced signal quality and capacity for extensive probe multiplexing permits quantitative analysis of distinct, highly intermixed cell populations in intact $C_e$3D-treated tissues via 3D histo-cytometry. We use this technology to demonstrate large-volume, high-resolution microscopy of diverse cell types in lymphoid and nonlymphoid organs, as well as to perform quantitative analysis of the composition and tissue distribution of multiple cell populations in lymphoid tissues. Combined with histo-cytometry, $C_e$3D provides a comprehensive strategy for volumetric quantitative imaging and analysis that bridges the gap between conventional section imaging and disassociation-based techniques.**

tissue clearing | quantitative microscopy | histo-cytometry | immune system

Major physiological processes rely on the precise positioning of diverse cell types in specific anatomical locations. Such organization allows exposure of cells to appropriate tissue microenvironments that shape their differentiation, promote appropriate cell–cell communication events, and collectively define the global properties of the whole organ. Understanding these structure–function relationships requires a detailed mapping of both the large-scale organization and fine-grained molecular and cellular composition of complex tissues.

The majority of information on such processes comes from microscopic imaging of relatively thin (5–20 μm) "2D" tissue cross-sections, examining several markers of interest to visualize a limited number of cell populations with respect to a tissue's representative structural elements. Although providing an excellent framework for understanding general features and the respective positioning of well-represented cell types, such data lack information on 3D organization, being particularly limiting for irregular structures such as the vasculature, airways, nervous tissue, inflamed sites, tumors, or reactive lymph nodes. Furthermore, detection and analysis of rare cellular events requires imaging of a large number of disconnected sections, which introduces possible image selection bias and suffers from the potential omission of key physiological landmarks located just outside of the sampled area. Finally, many cell types require simultaneous visualization of multiple phenotypic markers for correct subset identification, making interpretation of cell composition within tissues problematic without the use of highly multiplexed imaging panels.

Recently, several tissue clearing methodologies have been developed that render organs transparent and allow section-free imaging of significant volumes, thereby improving our capacity to study the relationships between cell positioning and 3D tissue architecture (1–11). These techniques work by reducing light scattering in tissues through minimizing refractive index mismatches between the immersion medium and the various protein, aqueous, and lipid tissue constituents (12). However, each of the currently reported clearing techniques suffers to a greater or lesser extent from various method-specific limitations. For example, techniques that excel at brain tissue clearing through lipid extraction suffer from limited compatibility with immunolabeling, while solvent-based methods that permit useful antibody-based immunofluorescence microscopy induce substantial tissue shrinkage and are associated with suboptimal signal quality (1, 2, 6, 7, 9). These limitations prevent assessment of a tissue's large-scale structural organization in concert with high-fidelity information on single cell morphology and complex molecular phenotype, while also limiting the combined use of fluorescent genetic markers and antibody-based staining.

One application that requires highly optimized acquisition of such information is histo-cytometry (13). This imaging/analysis pipeline allows multiplex phenotypic identification and quantification of cells directly in tissues, akin to in situ flow cytometry. This technique has been used to study the composition, distribution, and function of densely packed cells with complex phenotypes and morphology in tissue sections (13–21). Even for cell types with relatively simple morphology, such as T and B lymphocytes, histo-cytometry requires a high degree of spatial signal resolution, achieved with high numerical aperture (N.A.) objectives and deconvolution. The ability to simultaneously detect

## Significance

Major biological processes rely on the precise positioning of diverse cell types in specific anatomical locations. Existing techniques for studying cellular spatial positioning in tissues, especially with robust identification of densely packed cells, have substantial time, cost, resolution, and multiplexing limitations. Here, we describe an easy-to-use and inexpensive tissue clearing technique for attaining high-quality images of cells and diverse molecules of interest in substantial tissue volumes, enabling simultaneous quantitative analysis of 3D organ structure and fine-grained cellular composition. This technology will enhance our capacity for acquiring a quantitative understanding of the relationships between cells and their microenvironments in the context of broader tissue organization and is directly applicable to diverse biological disciplines as well as diagnostic medicine.

Author contributions: W.L., R.N.G., and M.Y.G. designed research; W.L. and M.Y.G. performed research; W.L. and M.Y.G. contributed new reagents/analytic tools; W.L., R.N.G., and M.Y.G. analyzed data; and W.L., R.N.G., and M.Y.G. wrote the paper.

Reviewers: M.K.J., University of Minnesota; and M.J.M., Washington University in St. Louis.

Conflict of interest statement: The initial patent for the methodology described in this paper was filed with the US Patent Office, E-Numbers: E-168-2016/0-US-01 Appl. Serial No.: 62/380,593, Title: "Clearing-enhanced 3d (ce3d): a novel tissue clearing method preserving cellular morphology, reporter fluorescence, epitope."

[1]To whom correspondence may be addressed. Email: rgermain@niaid.nih.gov or gernermy@uw.edu.

This article contains supporting information online at www.pnas.org/lookup/suppl/doi:10.1073/pnas.1708981114/-/DCSupplemental.

multiple distinct probes, achieved by multiplex labeling with directly conjugated antibodies, is critical for this technique, as it allows in-depth in situ phenotypic analysis, including definition of cellular lineages, analysis of ongoing signaling events through phosphoprotein detection, and delineation of functional states such as cytokine production (16). Furthermore, this analytical imaging approach can achieve more accurate cellular enumeration compared with disassociation-based flow cytometry, especially for highly adherent cell types (13, 22). However, our attempts to use histo-cytometry on organs cleared with existing techniques that permit modest multiplex antibody staining proved challenging due to relatively poor signal-to-noise characteristics and lack of clear-cut cellular definition (14).

Here, we describe a tissue clearing method, clearing-enhanced 3D ($C_e$3D). This technically nondemanding and inexpensive technique simultaneously achieves: excellent tissue transparency, maintenance of fluorescence from diverse reporter proteins and organic fluorophores, retention of cellular morphology, and a capacity for highly multiplexed antibody-based immunolabeling. $C_e$3D allows rapid clearing of most tissues, other than erythrocyte-dense organs rich in light-absorbing heme, and works well with lipid-rich brain tissues using additional mild detergent treatment. Here, we applied $C_e$3D to multiplexed confocal imaging of various lymphoid and nonlymphoid organs and cell types. The high signal quality and spatial resolution achieved with $C_e$3D allowed us to perform accurate quantitative analysis of cellular phenotypic profiles in dense lymphoid tissues using histo-cytometry, using optimized algorithms for cellular segmentation in 3D volumes. Collectively, this clearing technique and analysis pipeline provides a significant advance, attaining nearly lossless tissue transparency that supports large volumetric multiplexed microscopy and quantitative tissue cytometry.

## Results

**Optimization of a Clearing Protocol.** Recently described tissue clearing techniques have been valuable for visualization of macroscale 3D tissue architecture, suggesting that such approaches may also allow examination of the fine-grained relationships between various cell populations and their microanatomical surroundings. However, consistent with reports by others (2, 3, 8, 12), in our hands all major clearing methodologies (CUBIC, CLARITY, PACT, SeeDB, ClearT, ClearT2, Scale, AbScale, SWITCH, DISCO-based methods, BABB) failed to simultaneously yield optimal tissue transparency, bright reporter protein fluorescence, strong immunolabeling via directly conjugated antibodies, as well as minimally perturbed tissue and cellular morphology (*SI Appendix*, Figs. S1 and S2 *A* and *B* and Table S1). For some techniques, immunolabeling could be partially rescued via secondary reagent amplification, although this is problematic for extensive probe multiplexing with antibody clones derived from the same host species (*SI Appendix*, Fig. S2*C*). Considering the importance of all these parameters for accurate characterization of phenotypically and morphologically complex cells in large 3D volumes, we performed a chemical screen based on previous methods to find a clearing method that would satisfy the following criteria: tissue clarity, conservation of reporter protein fluorescence, optimal preservation of antibody-based staining for multiplex imaging, overall signal quality, morphological integrity at the cell and tissue level, minimal clearing time, and low reagent costs.

We began our search using 1% paraformaldehyde (PFA)-fixed murine lymph nodes (LNs). These tissues are ideal for such screening as they are (*i*) composed of diverse hematopoietic and stromal cell types with discrete phenotypic, morphologic, and spatial distribution properties; (*ii*) have cells that are densely packed, requiring a high degree of signal-to-cell spatial fidelity for quantitative image analysis; and (*iii*) are ≈1–2 $mm^3$, allowing rapid treatment followed by full volume imaging with conventional confocal objectives with reasonable N.A. One percent PFA, instead of 4%, was used to minimize epitope loss and improve tissue transparency. To further facilitate our search, we used tissues from Itgax-Venus (commonly known as CD11c-YFP) mice, which were fixed and then stained for 1–3 d with antibodies against various lymphocyte and stromal cell markers that have been well characterized to work with PFA-fixed tissues. This approach allowed us to ascertain a reagent's clearing properties together with its ability to retain signal from fluorescent proteins and permit antibody-based staining. It also provided information on preservation of fine cellular structures based on examination of morphologically complex dendrites of CD11c-YFP–expressing cells.

Solvent-based clearing approaches, such as BABB and different DISCO techniques, induce clearance at the cost of significant tissue shrinkage and loss of reporter protein fluorescence (1, 2, 9). Therefore, our primary screening was based on published aqueous passive immersion reagents, which on their own can reduce tissue light scattering. For this we compared various concentrations of Histodenz and fructose, previously described inexpensive immersion reagents that provide the ability to modulate the final refractive index through concentration adjustment (7, 11). As expected, immersion media alone only partially cleared the tissues. However, Histodenz was noted to be of substantially lower viscosity compared with fructose, allowing improved equilibration with the tissues, and was thus used for further screening of primary clearing reagents.

Comparison of various published aqueous primary clearing reagents demonstrated that formamide, a urea-like chemical used in the ClearT methodology (10), when combined with Histodenz induced exceptional transparency in treated tissues, while preserving YFP fluorescence and cell morphology. However, in our hands, antibody-based staining was poor with this treatment and did not permit imaging using the majority of tested antibodies, especially with directly conjugated probes (*SI Appendix*, Fig. S2 *A* and *B*). A secondary screen based on formamide's molecular structure was performed (*SI Appendix*, Table S2). Of the tested compounds, *N*-methylacetamide, 2-chloro-*N*-(hydroxymethyl)acetamide and *N*, *N*-dimethylacetamide yielded excellent optical tissue transparency within 12 h of tissue incubation at room temperature. However, only *N*-methylacetamide (22% wt/vol) in Histodenz (86% wt/vol) yielded tissue transparency with retention of reporter protein fluorescence and an ability to perform direct multiplex antibody-based immunolabeling (Fig. 1*A* and *SI Appendix*, Fig. S3). As commonly observed with other clearing protocols, some yellow/brownish tissue discoloration was noted, which was minimized by addition of 1-thioglycerol (0.5% vol/vol) (11). Finally, a mild detergent, 0.1% Triton X-100, was added to the final $C_e$3D clearing solution to expedite the clearing process.

Once optimal LN clearing was obtained with $C_e$3D treatment, we performed confocal imaging of both reporter proteins and various epitopes labeled with directly conjugated antibody probes. The ∼650-μm working distance of a 20× 0.75-N.A. objective coupled with motorized stage tiling allowed us to image the entirety of smaller LNs using a conventional confocal microscope. Various hematopoietic and nonhematopoietic cell types were easily visualized throughout the whole ∼650-μm imaging range with excellent signal fidelity (Fig. 1*B* and *SI Appendix*, Fig. S3). Clear-cut demarcation of B cells, dendritic cells, T cells, and lymphatic endothelium was seen, with the appropriate tissue-level compartmentalization (*SI Appendix*, Fig. S3). These results suggested that $C_e$3D achieves LN tissue transparency, preserves YFP reporter protein fluorescence, and is generally compatible with antibody-based immunofluorescence microscopy.

We next examined the performance of $C_e$3D for clarification and imaging of other major mouse organs. We observed robust clearing of lung, intestine, liver, muscle, and thymus, as well as preservation of reporter protein fluorescence in these organs (Fig. 1 *C* and *D* and see below). Similarly, $C_e$3D treatment of

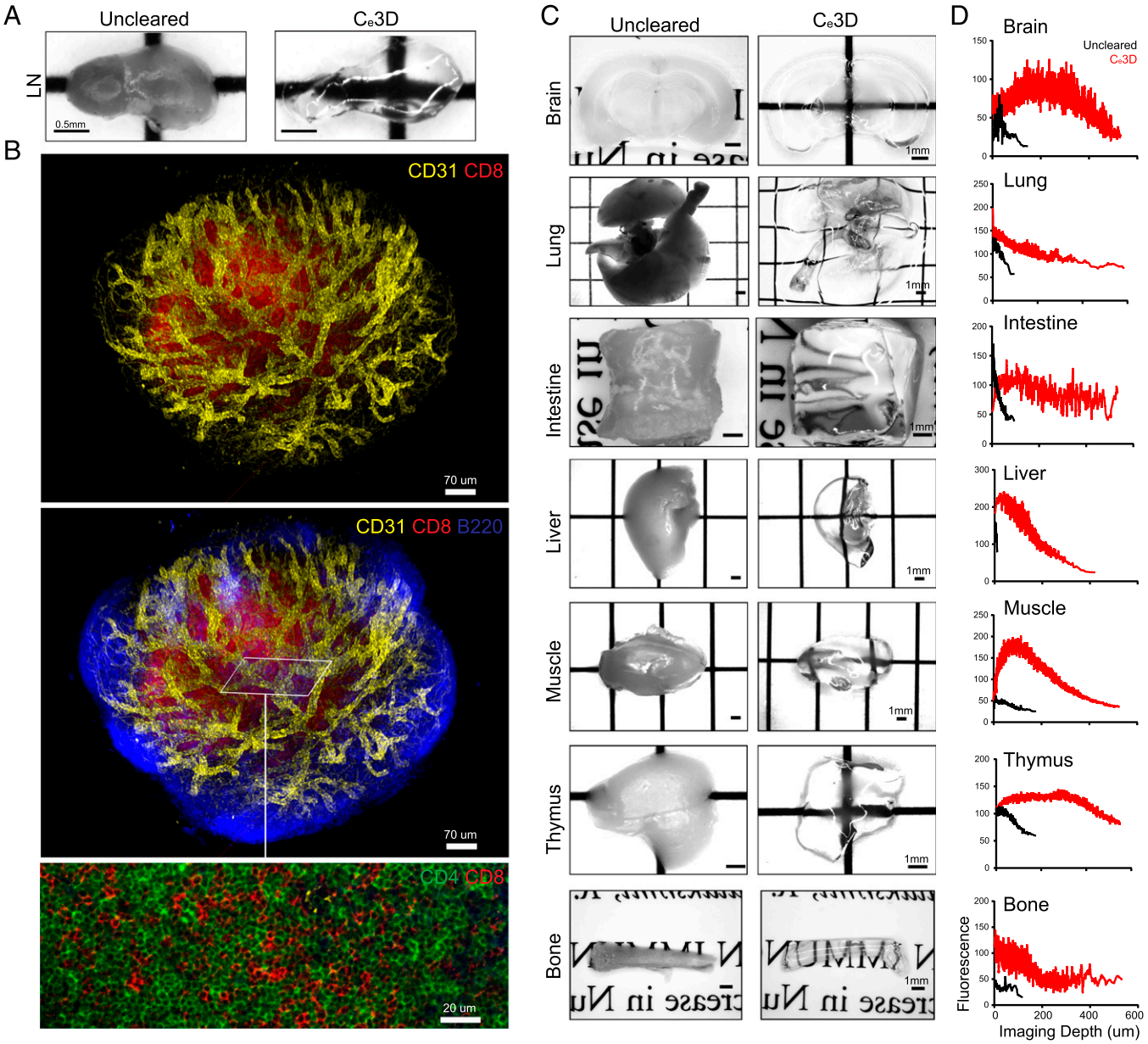


**Fig. 1.** $C_e$3D attains tissue transparency while retaining reporter protein fluorescence and capacity for immunolabeling. (*A*) Images of fixed LNs were acquired before (PBS) and after $C_e$3D treatment. (*B*) LNs were stained with the indicated antibodies, cleared with $C_e$3D, and imaged by confocal microscopy, with the zoom-in panel (*Bottom*) demonstrating the capacity to resolve individual cells. (*C*) Images of various murine organs were acquired before and after $C_e$3D treatment. (*D*) Average cellular fluorescence for CD11c-YFP–expressing cells across indicated imaging depths was quantified for PBS (black) or $C_e$3D (red) -treated tissues. Laser power ramping and signal attenuation correction was not used for quantitative comparison of fluorescence detection. Images represent at least two independent experiments.

bone samples demonstrated rapid gain of transparency for entire femurs without necessitating decalcification, suggesting that dense connective tissues are also compatible with this technique. Kidneys could also be cleared and imaged with $C_e$3D, but required extensive portal vein perfusion (*SI Appendix*, Fig. S4*A*). Only the spleen that is exceptionally rich in erythrocytes did not achieve optical transparency with $C_e$3D in our studies, presumably due to the preservation of heme's molecular structure and its light absorbing characteristics. Brain tissues rich in lipids also gained transparency, but required substantially longer incubation times in the clearing medium (≈2 wk per 1 mm of tissue). To minimize this lag time, we explored various detergents for enhancing lipid removal and found that commercial saponin-based fixation and permeabilization flow cytometry buffers promoted dramatically faster rates of brain tissue clearing (~24 h per millimeter of tissue), while also maintaining the capacity for antibody-based immunolabeling (Fig. 1*C*, see below).

To quantitatively assess the effective light transmittance gained with $C_e$3D treatment, we measured the fluorescence in YFP-expressing cells in various tissues using a fixed laser/detector power setting throughout the working range of the objective. As expected, uncleared organ imaging resulted in rapid decay of signal detection within the first 50 μm of imaging. In contrast, minimal signal attenuation was observed over the first 200 μm in $C_e$3D-treated tissues, although beyond that depth, residual light scatter did result in decreased signal intensity (Fig. 1*D*).

In practice, however, such attenuation could be easily corrected with a minor laser power ramp (~2–3× laser intensity increase across 650 μm), as well as further optimized by software-based attenuation correction algorithms after image acquisition, allowing for productive, high-quality imaging throughout the entire 650-μm working distance range of the objective (Fig. 1*B* and *SI Appendix*, Fig. S3).

Tissue deformation and morphological distortions are common artifacts observed with clearing protocols (12). $C_e$3D induced minimal change in volume for many tested organs, although some shrinkage (10–20%) was observed for select tissues, such as brain, gut, and muscle (*SI Appendix*, Fig. S4*B*). To examine whether such shrinkage would influence cellular morphology, we compared the morphology of astrocytes, cells with fine processes, in untreated brain slices vs. in tissues cleared with the different methodologies. This approach was taken because brains demonstrated the most discernible volumetric contraction and the astrocyte-specific GFAP antibody has been previously reported to work with a variety of clearing techniques, allowing direct method comparison. Indeed, astrocyte labeling was observed with all tested techniques, although iDISCO treatment resulted in reduced fluorescent signal detection (*SI Appendix*, Fig. S4*C*). Importantly, $C_e$3D led to an overall preservation of astrocyte integrity and morphological complexity compared with cells in noncleared control thin sections. In contrast, substantial shrinkage and rounding, as well as noticeable serration of cellular processes, was observed with iDISCO-based clearing. Some serration was also noticeable with PACT clearing. To further assess the effect of $C_e$3D on cell morphology, we visualized neuronal cell bodies using brain tissues isolated from Confetti reporter animals (see below). Although shrinkage of the cell bodies (12–15%) was observed, consistent with the change in organ volume, the overall neuronal morphology appeared intact, while the improved fluorescent reporter signal detection due to optical clearing led to enhanced visualization of fine axonal processes (*SI Appendix*, Fig. S4*D*). Furthermore, we examined the morphology of myeloid dendritic cells in LNs and small intestines, and observed no significant alterations in cell shape and volume before and after $C_e$3D clearing (*SI Appendix*, Fig. S4*E*). Finally, we observed no evidence of differential regional deformation within the cleared tissues, as the relative diameter of cells remained unchanged within different tissue sites, suggesting overall uniformity of volumetric contraction during the clearing process. Collectively, these data indicate that although $C_e$3D does lead to modest tissue shrinkage in certain organs, it preserves excellent morphological integrity, and due to improved signal detection, allows enhanced visualization of fine cellular processes.

To test the compatibility of $C_e$3D with various commonly used fluorescent reporter proteins, we examined tissues from Confetti reporter mice, which express GFP, RFP, YFP, and CFP in distinct cells. $C_e$3D treatment led to preservation of fluorescence for these reporters, as well as to improved detection of these proteins, with tissues stored in $C_e$3D medium retaining fluorescence for more than 4 wk (*SI Appendix*, Fig. S5*A*). Similar results were observed for DsRed-expressing tissues (*SI Appendix*, Fig. S4*A*). Next, we tested how well $C_e$3D enables combined use of antibody-based and reporter protein imaging by comparing the staining intensity of labeled antibodies against distinct B- and T-cell markers before and after $C_e$3D treatment of thin CD11c-YFP tissue sections. Both lymphocyte populations were detected in the physiologically appropriate compartments, with antibody-stained and YFP-expressing cells showing the same or better fluorescence signal detection after $C_e$3D treatment (*SI Appendix*, Fig. S5*B*). Further testing of multiple fluorophore-conjugated antibodies against diverse biological targets and in various tissues also demonstrated similar performance to that seen with PFA-fixed, noncleared tissue sections, suggesting good preservation of antibody–antigen complexes with $C_e$3D (*SI Appendix*, Table S3). Moreover, all fluorophores commonly used in immunolabeling that we tested were compatible with the $C_e$3D protocol, retaining stable fluorescence for several weeks after clearing (*SI Appendix*, Table S3).

Volumetric imaging of reporter protein expressing and antibody-stained tissues after $C_e$3D processing revealed at high resolution the complex relationships of diverse cell types with tissue-specific anatomical landmarks. As an example, small intestines from CD11c-YFP reporter animals allowed visualization of the spatial associations between the densely packed epithelial cells, intraepithelial lymphocytes, lymphatic vessels, and dendritic cells (Fig. 2*A* and *SI Appendix*, Fig. S6*A* and Movie S1). Cleared 1-mm brain slices from Confetti animals allowed 3D visualization of neurons (Fig. 2*B* and Movie S2), while GFAP-stained CD11c-YFP brain tissues demonstrated fine morphological processes for astrocytes and dendritic cells, respectively, and imaging of cleared Cx3CR1-GFP reporter brains revealed fine branching of ramified microglial cells (Fig. 2*C* and *SI Appendix*, Fig. S6 *B* and *C* and Movie S3). Furthermore, complex 3D networks of blood vessels in the brain were revealed using DsRed reporter animals (Fig. 2*D* and Movie S3). Large volumetric scans of diverse CD11c-YFP tissues permitted visualization of additional cellular anatomical relationships, such as close associations of dendritic cells with lung alveolar epithelium, as revealed by either confocal or light sheet imaging (Fig. 2 *E* and *F* and *SI Appendix*, Fig. S6*D* and Movie S4), dense dendritic cell aggregates in thymic medullary regions, and close associations of YFP-expressing Kupffer cells with liver sinusoids (*SI Appendix*, Fig. S6 *E* and *F*). Similarly, cleared dsRed femurs allowed high-resolution confocal imaging of blood vessels within the calcium-rich periosteum (Fig. 2*G*). Collectively, these results demonstrate that $C_e$3D achieves tissue transparency with preservation of overall tissue and cellular integrity in a variety of organ systems and is compatible with fluorescent reporter proteins and antibody-based labeling, thus allowing comprehensive high-resolution imaging across large tissue volumes.

**Quantitative Volumetric Cell-Level Analysis Using $C_e$3D and Histo-Cytometry.** This simultaneous high degree of signal quality, capacity for extensive probe multiplexing, and preservation of cellular morphology obtained with $C_e$3D imaging suggested that 3D quantitative histo-cytometry might also be feasible. This technique extracts statistical information for imaged cells, such as the associated fluorescent intensity, cellular morphological properties, and position (13). This in turn allows software-based comparison and population gating of cells, akin to in situ flow cytometry, with the major added benefit of retaining information on cellular spatial distribution in tissues. Previous cell segmentation techniques, necessary for identifying individual cells within an image, used either more restrictive segmentation of a single cell type (e.g., CD11c-YFP signal-based segmentation), or nuclear stain-based segmentation for all nucleated cells (13). As the latter approach effectively provides quantitative information on all imaged nucleated cells and not just select subpopulations, we first attempted to perform whole-mount nuclear staining for nuclear-based segmentation. However, substantial inhomogeneity in nuclear labeling was observed, with significantly greater staining in peripheral regions of dye-incubated tissues. Modifications to dye concentrations, the choice of probe (e.g., DAPI, Hoechst, Yoyo-1, Jojo-1, and ToPro-5), or labeling time failed to normalize staining intensity across tissues. Nuclear segmentation of tissues from histone GFP-tagged reporter animals also failed to produce accurate results due to significant cellular heterogeneity in nuclear fluorescence. To circumvent these issues, we explored various image processing pipelines to accurately segment all imaged cells independent of nuclear staining. Effective cell object creation was achieved via seeded watershed segmentation of a calculated channel representing the inverse sum of all membrane signals (Fig. 3*A*). Additional enhancements of cell separation and segmentation

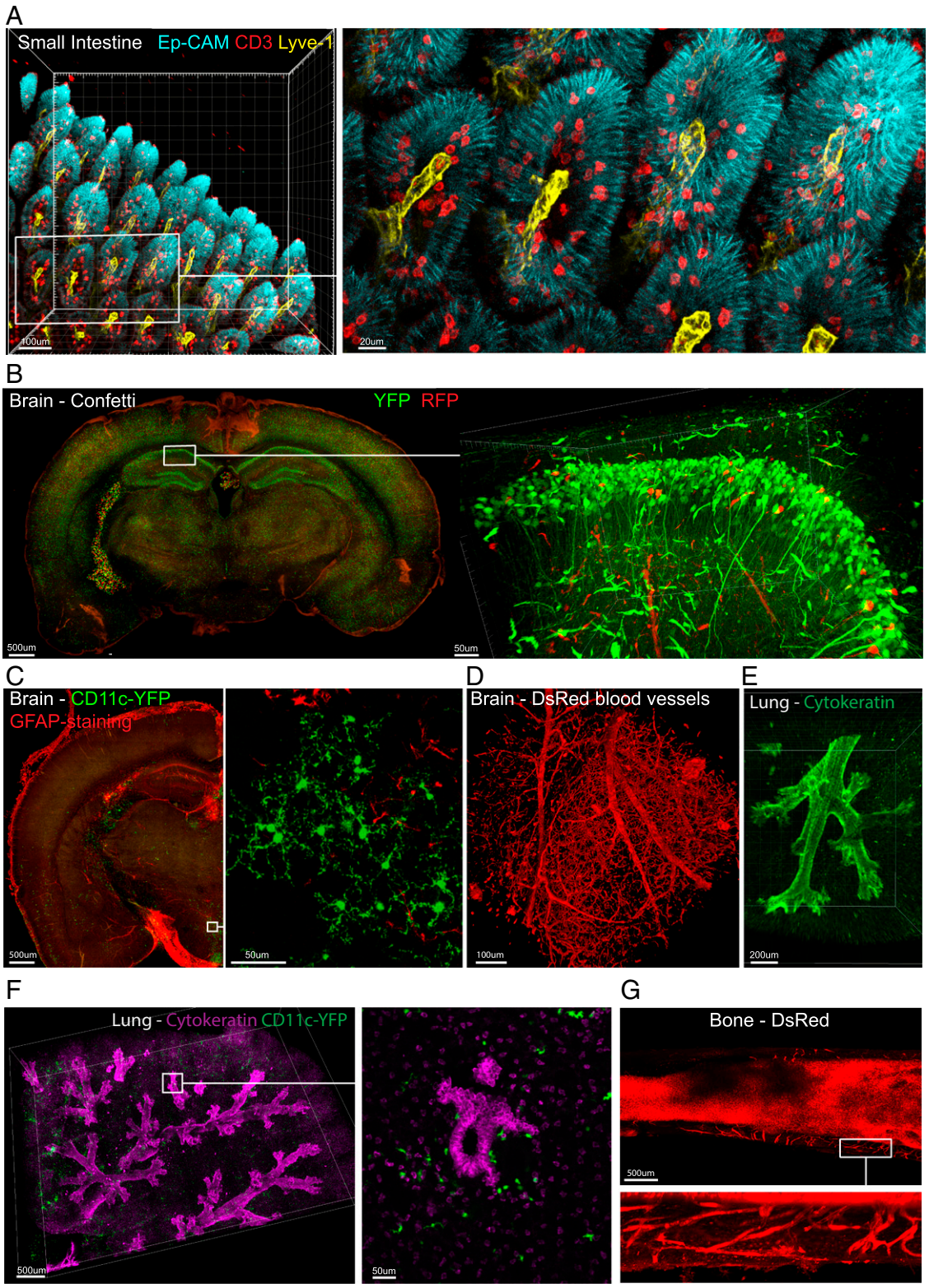


**Fig. 2.** Large volumetric $C_e$3D microscopy of diverse organs. (*A*) Segments of the proximal small intestine were stained with the indicated antibodies, cleared and imaged, allowing visualization of the spatial relationships between the mucosal epithelium (EpCAM$^+$, cyan), T cells (CD3$^+$, red), and lymphatics (Lyve-1$^+$, yellow). (*B*) $C_e$3D-processed 1-mm Confetti reporter brain slices were imaged, allowing visualization of neuronal processes and blood vessels. (*C*) GFAP-stained CD11c-YFP brain slices demonstrate compatibility of reporter and immunolabeling-based fluorescence, as well as preservation of cell morphology with $C_e$3D. (*D*) Cleared DsRed reporter brain tissues allow visualization of complex vascular networks. Cytokeratin-stained lungs from CD11c-YFP mice allow 3D visualization of bronchial epithelial cells and dendritic cells via light-sheet (*E*) or confocal (*F*) microscopy. (*G*) Visualization of periosteal blood vessels within actin-DsRed $C_e$3D-cleared femurs. Images represent at least two independent experiments.

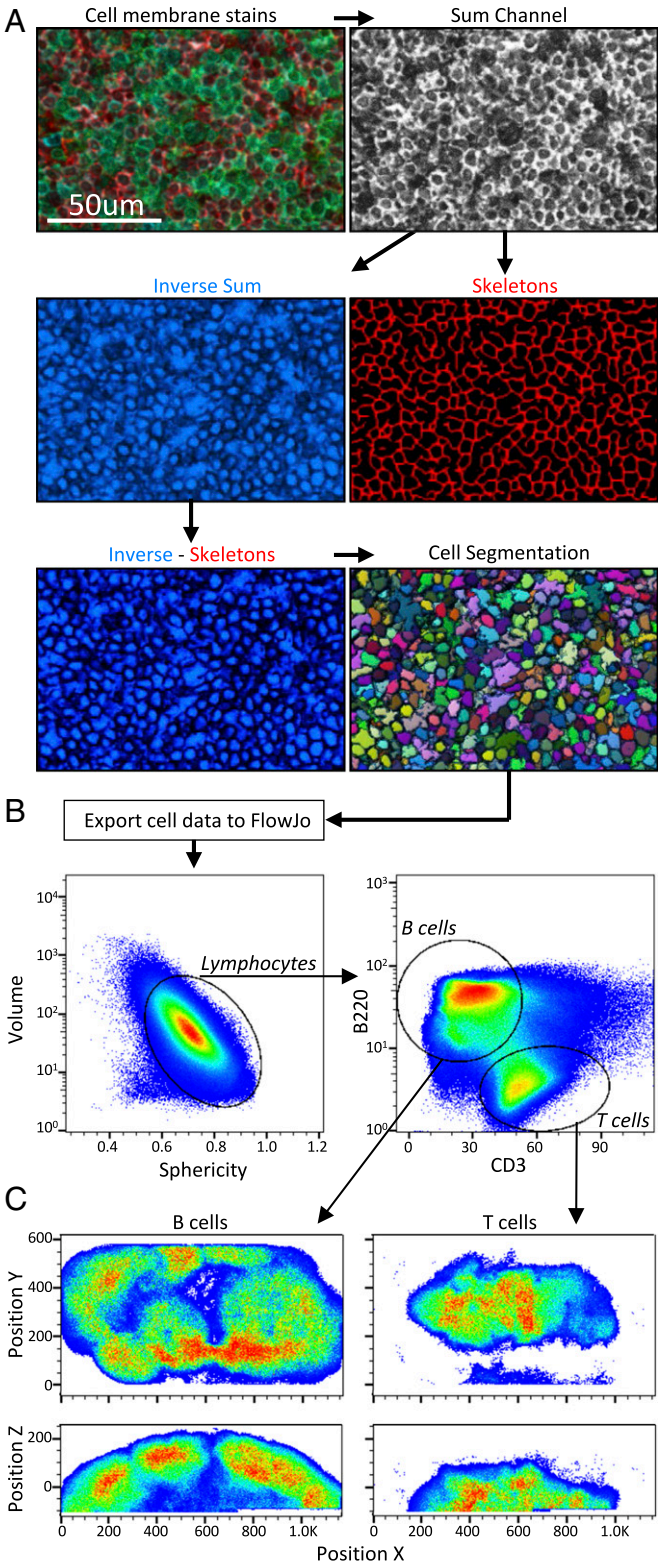


**Fig. 3.** Volumetric segmentation pipeline for quantitative tissue analysis. (*A*) Cell membrane stains were normalized by intensity and summed together to yield the sum channel. This channel was then inverted to create an inverse sum channel and used to create 2D skeletons in the XY, XZ, and YZ planes. These skeletons were then subtracted from the inverse sum channel to enhance the separation between cells. This enhanced image was then segmented to create individual cell objects. (*B*) The statistics for the cell objects were exported into FlowJo for cellular phenotyping and population gating. (*C*) Positional information on gated cell populations was used to quantitatively visualize cellular position. Data are representative of at least three independent experiments.

were attained by creating binary skeleton channels derived from the sum of membrane signals, and then by subtracting these from the inverse sum channel. Exporting statistics data for the segmented cell objects into flow cytometry analysis software (FlowJo) and plotting mean voxel fluorescence intensity allowed robust discrimination of various lymphocyte populations based on marker expression (Fig. 3*B*). Importantly, analysis of the cellular position of the gated cell types revealed physiologically appropriate localization in LN tissues (23, 24), with positioning of B cells in the peripheral follicular regions and with T cells concentrated in the central T-cell zone (Fig. 3*C*).

To further examine whether $C_e$3D volume imaging would allow histo-cytometric analysis of multiple cell populations, LNs were stained with a multiplexed panel of antibodies against diverse hematopoietic and stromal cell types, cleared, and imaged with a 20× 0.75 N.A. objective. Collected images were compensated for fluorescence spillover between channels, deconvolved to enhance spatial signal allocation, and corrected for signal attenuation in the axial plane. Three-dimentional image visualization revealed the highly branched organization of the blood and lymphatic vessel networks, along with their relationships to the B-cell follicles and T-cell zones within LNs (Fig. 4*A* and *SI Appendix*, Fig. S7*A* and Movie S5). We next performed cellular segmentation and exported cell object statistics to FlowJo software for quantitative cellular analysis (Fig. 4*B* and *SI Appendix*, Fig. S7*B*). Large, irregular events or objects lacking cell-associated signal (sum of cell membrane channel) were eliminated from further evaluation. $CD31^+$ blood endothelial cells (BECs), $Lyve1^+$ lymphatic endothelial cells (LECs), $CD169^+$ subcapsular sinus macrophages (Macs), B cells, and T cells were readily identified in a hierarchical gating analysis (Fig. 4*C*). Importantly, XYZ positioning for all gated cell populations precisely mirrored the original image dataset and the expected physiological compartmentalization (23, 24), suggesting accurate cellular segmentation, analysis, and spatial allocation (Fig. 4*D* and Movie S6).

One area of concern was that many LECs appeared to show expression of CD169, a marker typically associated with LN macrophages (25) (Fig. 4*C*). Closer image examination revealed extremely tight association of medullary macrophages and LECs, with the CD169 and Lyve-1 signals not readily separable using the 0.75 N.A. optics, especially in the axial plane (*SI Appendix*, Fig. S7*A*, cross-section zoom). Such signal misallocation would thus lead to inaccurate phenotypic characterization of LECs with histo-cytometry. These results suggested that higher N.A. objectives may be necessary for accurate phenotypic characterization of closely juxtaposed cells, as was previously observed in section-based histo-cytometry analysis of dendritic cells and T cells (13). Indeed, use of 40× 1.3 N.A. optics, with further enhancement by deconvolution, readily separated juxtaposed macrophages and LECs in the axial and lateral planes and allowed accurate quantitative histo-cytometry of LECs and macrophages (*SI Appendix*, Fig. S7 *C* and *D*).

To further probe the fidelity of $C_e$3D histo-cytometry for closely proximal cells, we examined whether phenotypic characterization of $CD4^+$ and $CD8^+$ T cells could be achieved. These T-cell populations are tightly packed within the LN T-cell zone and do not share expression of the CD4 and CD8 coreceptor markers, thereby providing an excellent opportunity for testing the $C_e$3D histo-cytometry pipeline (Fig. 5*A* and *SI Appendix*, Fig. S8). Recent section-based image analysis has revealed a more fine-grained microanatomical organization of the T-cell zone, with immunologically experienced $CD44^+$ memory T-cell populations

predominantly residing in the interfollicular regions, and with regulatory $CD4^+CD25^+$ T cells dispersed throughout the T-cell zone but also occasionally localized in tight clusters in the peripheral regions of the LN paracortex (16, 26, 27). Staining of LN tissues with the appropriate antibody panels followed by $C_e$3D imaging and histo-cytometric analysis allowed discrimination of

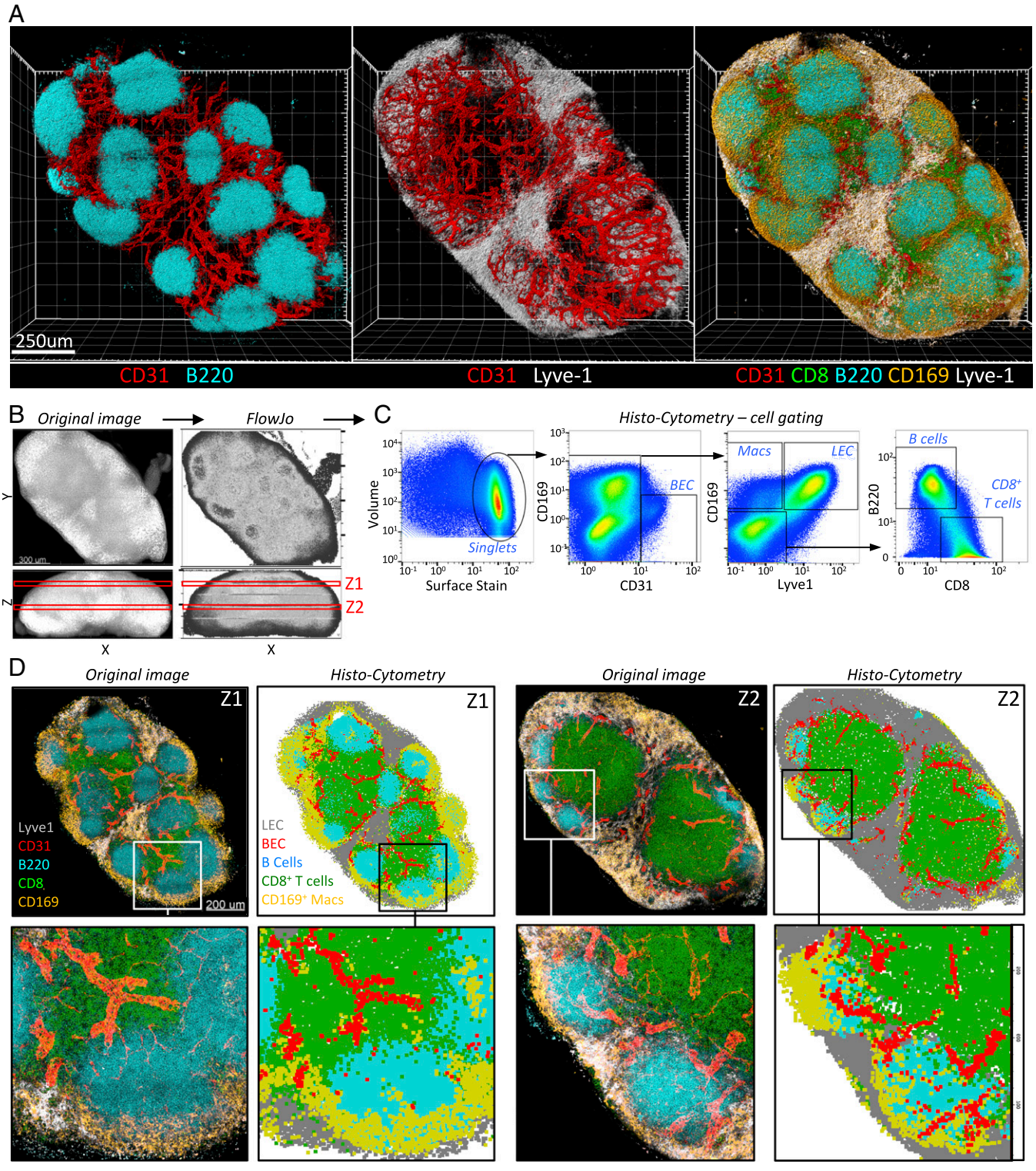


**Fig. 4.** $C_e$3D permits volumetric multiplex imaging and quantitative histo-cytometry. (*A*) LNs were stained with the indicated antibodies, cleared, and imaged with a 20× 0.7 5 N.A. objective. (*B*) Cell membrane signals were used to create cell objects, which were then exported into FlowJo. The 3D organ reconstruction in FlowJo is presented and compared with the original image. (*C*) Cell object statistics were used for population phenotypic analysis and gating of blood endothelial cells (BECs), lymphatic endothelial cells (LECs), macrophages (Macs), as well as B and T cells. (*D*) Gated cell populations from *C* were displayed on an XY positional plot for the Z-dimension gates defined in *B* (red rectangles) and compared with the same Z planes from the original image. Images are representative of at least two independent experiments.

all cellular populations of interest, such as B cells, and importantly CD4$^+$ and CD8$^+$ T cells, with little marker overlap, suggesting that the 1.3 N.A. optics allowed accurate signal–cell allocation during image segmentation (Fig. 5 *B* and *C*). CD44$^+$ memory T cells and CD25$^+$ regulatory CD4$^+$ T cells were also detected at the expected frequencies and displayed previously

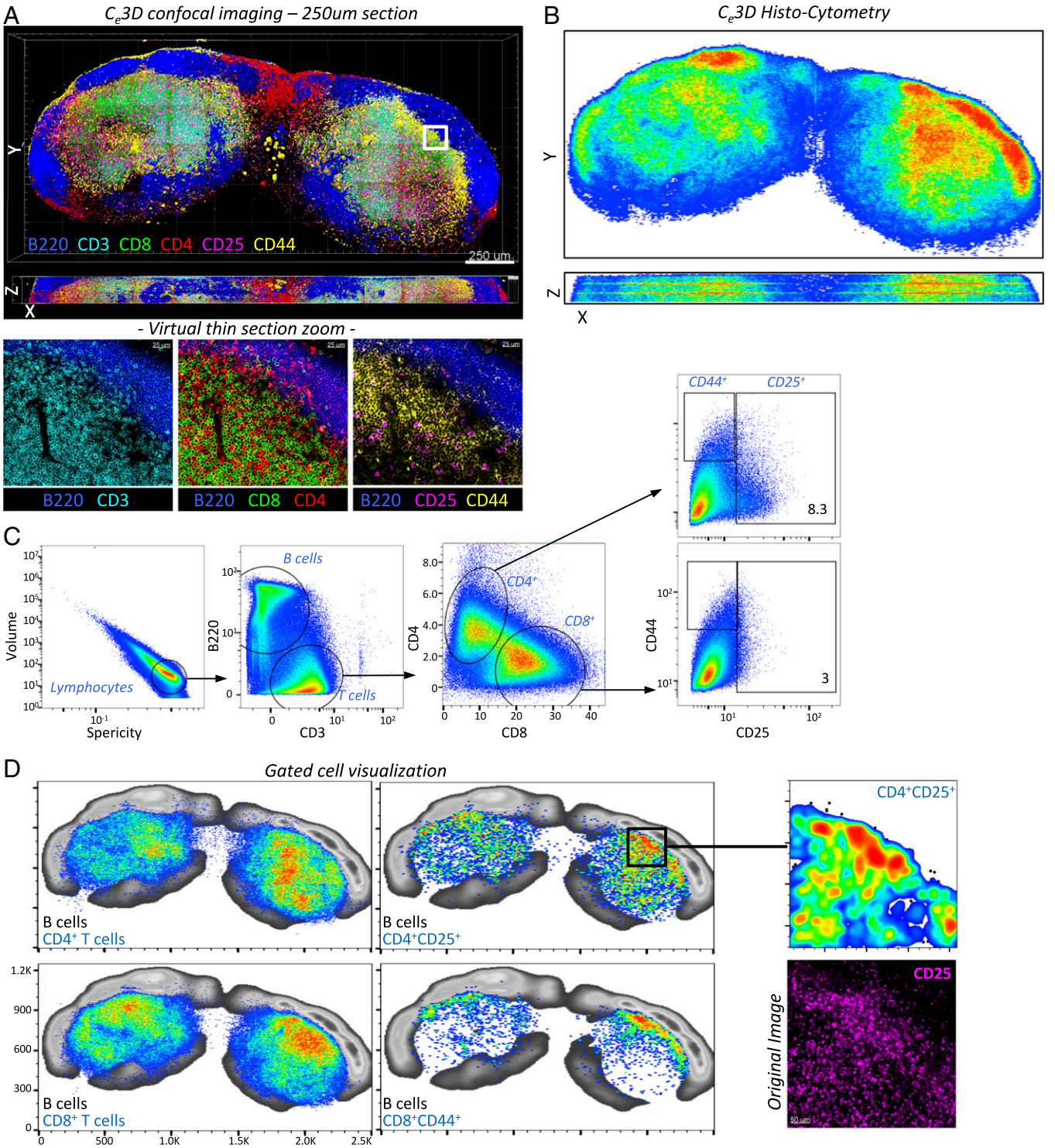


**Fig. 5.** C$_e$3D histo-cytometry of closely adjoining cells in large tissue volumes. (*A*) LNs were stained with the indicated antibodies, cleared, and imaged with a 40× 1.3 N.A. objective (*Top*). A zoom-in image, corresponding to a single virtual Z section within the area highlighted by the white box (*Top*), demonstrates the visual clarity of various lymphocyte subpopulations (*Bottom*). (*B*) All imaged cells were segmented and their statistical information was exported into FlowJo for quantitative tissue visualization, as well as (*C*) population phenotypic analysis and gating. (*D*) Indicated T-cell populations were displayed as pseudocolor density XY positional plots, with the B cells superimposed (gray density gradients) to highlight regionalized cell distribution. Zoom-in image demonstrates an area enriched in CD4$^+$CD25$^+$ cell clusters, with the original microscopy image presented below. Images are representative of at least two independent experiments.

described nonhomogeneous distribution, with more predominant localization of memory T cells in the interfollicular zones, and with dispersed but sometimes clustered regulatory T-cell positioning in peripheral regions (Fig. 5 *C* and *D* and *SI Appendix*, Fig. S8).

One limitation of conventional confocal objectives for obtaining high-quality image datasets is the substantially shorter working distances, which restrict extensive volumetric microscopy. Recent developments of new objectives designed for cleared tissues have yielded optics with both high N.A. and large working distances. A close correspondence between the refractive index of $C_e$3D medium and the optimal immersion medium of the 25× 1.0 N.A. motCORR objective allowed us to examine the ability of $C_e$3D cleared organs to generate high-quality datasets across much larger tissue volumes. Indeed, using this objective to image $C_e$3D cleared mouse lung tissues, stained with an anti-cytokeratin antibody, we effectively visualized lung epithelial cells with clear-cut definition of cellular membranes to a depth of 3 mm (*SI Appendix*, Fig. S9). These data indicate that use of such specialized objectives with $C_e$3D cleared tissues will permit much larger volumetric quantitative microscopy of tissue samples from diverse species and organs. Collectively, these results indicate that the $C_e$3D imaging and histo-cytometry pipeline allows robust quantitative analysis of cellular states and distribution directly in 3D organs, including tissues with exceptionally high cellular densities and phenotypic complexities (*SI Appendix*, Fig. S10).

## Discussion

Valuable imaging of large tissues, such as entire mouse brains, has been achieved using available clearing methods (12). However, these analyses typically are conducted with low power, low N.A. objectives, thus producing images of modest resolution unsuited to fine-grained, highly-multiplex dissection of densely packed cells, such as the diverse cell populations of the innate and adaptive immune system (13, 28). Here, we describe a tissue clearing technique, $C_e$3D, that results in rapid and robust tissue transparency for most organs and is fully compatible with a wide assortment of reporter proteins and antibody-associated fluorophores, allowing multiplexed imaging of diverse analytes of interest in large (>2–3 mm thick) tissue volumes at high resolution. Furthermore, we provide an enhanced pipeline for cell segmentation and quantitative analysis, $C_e$3D histo-cytometry, which supports detailed exploration of cellular phenotypic and functional states in such 3D datasets (*SI Appendix*, Fig. S10). Collectively, these tools allow comprehensive dissection of the structure–function relationships involving diverse cell types with their surrounding microenvironments, effectively bridging the gap between imaging and quantitative cytometry.

$C_e$3D is conceptually based on several recent tissue clearing technologies, which have reignited interest in volumetric organ imaging, but have also been associated with certain limitations (12) (*SI Appendix*, Table S1). For example, solvent-based clearing quenches reporter protein fluorescence and leads to tissue shrinkage (1, 2, 9). On the other hand, urea-based hyperhydration causes tissue swelling and disruption of antibody–antigen interactions (4, 5). The newest generation urea-based method minimizes the latter issues, but necessitates use of a complex series of extended incubation steps, while still resulting in suboptimal epitope labeling and quenched protein fluorescence (3). In contrast, passive clearing techniques use incubations in simple high refractive index media, but do not result in optimal tissue transparency (10, 11). Hydrogel-embedding methods, which remove tissue lipids, can result in extensive protein cross-linking and poor epitope-based immunolabeling (6, 7). A recent glutaraldehyde-based method successfully demonstrated volumetric multiplexed imaging, but uses suboptimal fixation reagents and extreme pH treatments that can compromise antibody-based labeling and increase tissue autofluorescence, while also requiring multiple time-intensive incubation steps and complex 3D image registration algorithms (8). The $C_e$3D technology reported here is largely devoid of these limitations, inducing rapid optical transparency in most tissues using simple and inexpensive reagents and permitting high-quality, multiplexed, large volumetric microscopy of cells with varied morphology and phenotypic complexity in structurally intricate organs. While we did observe some decrease in tissue volume after $C_e$3D treatment of certain organs, most notably the brain, this shrinkage was not associated with apparent loss of morphological detail, and actually promoted discrimination of the fine cellular processes. Importantly, the obtained image quality was similar to gold-standard section-based imaging, with the major benefit of allowing volumetric tissue reconstruction or examination of samples in any preferred plane of interest. The latter is important as it reduces the undersampling errors associated with conventional thin sections taken at arbitrary angles through samples with asymmetric cell distributions, for example, a tumor with an immune infiltrate.

The compatibility of $C_e$3D with immunolabeling and a wide array of fluorophores provides a high degree of flexibility in reagent choice, and more importantly permits routine probe multiplexing using traditional confocal instruments equipped with spectral detectors. Considering the necessity for robust quantitation of such multidimensional datasets, we also developed an enhanced technique for 3D image segmentation and quantitative cellular analysis. The described $C_e$3D histo-cytometry pipeline is based on the previously described methodology for section-based imaging, with enhancements for segmentation of all imaged cells in large 3D datasets, irrespective of nuclear staining (13). It is based on commercial and open source software platforms and thus can be readily applied in diverse settings. One caveat is that even with this improved algorithm, some errors in enumeration can occur with cells of complex shape; we estimate the error to be on the order of 10–15% for cell types like myeloid dendritic cells, but this error is substantially smaller than that accompanying incomplete tissue extraction and enumeration by flow cytometry (13, 22).

Several roadblocks currently hinder large-scale adoption of volumetric quantitative imaging. The high molecular weights of antibodies and certain fluorophores necessitate long incubation times and often result in inhomogeneous tissue staining. Use of Fab antibody fragments, aptamers, or camelid-derived single chain antibodies conjugated to small organic fluorophores should improve tissue penetration and staining homogeneity (12). Pulsed vibrational energy with microwave technology may also promote reagent penetration into tissues (29). Furthermore, although conventional confocal microscopes allow high-resolution imaging of tissues, point-by-point raster scanning with high magnification optics necessitates significant time for acquisition of large volumetric datasets. For example, imaging of relatively small ~1-$mm^3$ LNs with a 20× objective, with multiple tiled stacks and several sequential scans for detection of multiplexed fluorescent probes, necessitates hours of microscope time per tissue sample. Current developments in light-sheet microscopy are likely to resolve this limitation in the near future, although a combination of high-speed and high-resolution imaging across such large tissue volumes is yet to be demonstrated with this technology (12, 30) (Fig. 2*E*). Further, the use of conventional high N.A. objectives is associated with significantly shorter working distances, thereby limiting the overall accessible image volume. The 20× objective used for the majority of imaging in this study allowed an effective imaging depth of up to 650 μm, but was suboptimal for accurate signal–cell allocation in the axial plane for closely adjoining, morphologically complex cells. Although these issues were resolved with the 40× 1.3 N.A. objective, its working distance was limited to less than 250 μm. Of note, even such a relatively limited depth provides an effective 10- to 30-fold increase in the amount of acquired information over traditional thin-section microscopy.

Importantly, recently developed microscope objectives designed for cleared tissues attain both high N.A. and large working distances (>5 mm), although such optics are currently limited to specific immersion media. We were able to examine the performance of one of these objectives with $C_e$3D-cleared tissues and obtained images with high signal-to-noise characteristics at 3-mm tissue depths, suggesting that such optics will aid in large volume, high-resolution imaging.

In addition to imaging constraints, computational requirements for quantitative analysis of large volumetric datasets are currently demanding, necessitating use of dedicated workstations with large amounts of RAM, as well as of specialized software tools, which when commercial, are quite expensive. Although successful cellular segmentation was achieved with the $C_e$3D histo-cytometry pipeline, limitations in parallel processing in the segmentation software available to us necessitated processing of very large image datasets as separate fragments. Such limitations are likely to be temporary, as substantial interest in large 4D datasets obtained with light-sheet microscopy has promoted development of novel open-source solutions for data handling and analysis of extremely large datasets (31, 32). Finally, commercially available fluorophores with distinctly separable excitation or emission spectra currently limit the number of probes to a maximum of 8–15. Although certain thin-section imaging approaches entailing repeated antibody labeling have demonstrated more extensive multiplexing, these will likely not be directly applicable without modification to large tissue volumes due to temporal requirements for reagent penetration (33, 34). Even with these limitations, powerful statistical or machine learning methods will be needed for better understanding of the complex relationships between cells and their surroundings as revealed by these imaging methods.

## Methods

**Mice.** CD11c-YFP [*B6.Cg-Tg(Itgax-Venus)1Mnz/J*], actin-DsRed [B6.Cg-Tg(CAG-DsRed*MST)1Nagy], Cxcl12-DsRed (*Cxcl12tm2.1Sjm/J*), Cx3cr1-GFP (B6.129P-*Cx3cr1tm1Litt/J*), and histone GFP-tagged reporters [B6.Cg-Tg(HIST1H2BB/EGFP)1Pa] were obtained from The Jackson Laboratory. Fluorescent Confetti animals were generated by crossing B6.129P2-Gt(ROSA)26Sortm1(CAG-Brainbow2.1)Cle/J × B6.Cg-Tg(UBC-cre/ERT2)1Ejb/2J (The Jackson Laboratory). Mice heterozygous for both transgenes were injected i.p. with tamoxifen 100 μg per gram of body weight in peanut oil (Sigma-Aldrich) for 5 consecutive days, with tissues collected on the fifth day for processing. Two- to 6-mo-old male/female mice were used for all experiments and were randomly allocated into treatment groups. The investigators were not blinded to allocation during experiments and outcome assessment. All mice were maintained in specific pathogen-free conditions at an Association for Assessment and Accreditation of Laboratory Animal Care-accredited animal facility at the National Institute of Allergy and Infectious Diseases (NIAID). All procedures were approved by the NIAID Animal Care and Use Committee (NIH).

**Microscopy and $C_e$3D Pipeline.** Detailed methods for $C_e$3D-tissue clearing, imaging, segmentation and quantitation, as well as other non-$C_e$3D methods examined in this report are provided in *SI Appendix, SI Methods*.

**Statistical Analysis.** Statistical tests were selected based on appropriate assumptions with respect to data distribution and variance characteristics. No statistical methods were used to predetermine sample size. The statistical significance of differences in mean values was analyzed by a two-tailed Student's *t* test. Paired *t* tests were conducted for comparison of the same tissue samples before and after $C_e$3D treatment. $^{***}P < 0.0001$, $^{**}P < 0.005$, and $^{*}P < 0.05$.

**ACKNOWLEDGMENTS.** We thank Dr. Andrea Radtke for providing tissues from Confetti reporter animals; Dr. Kairui Mao for helping with gut tissue preparation; all members of the Lymphocyte Biology Section, Laboratory of Systems Biology, National Institute of Allergy and Infectious Diseases (NIAID), NIH for many helpful comments during the course of these experiments; and Drs. Kerry Casey, Andrea Radtke, Kerry Mao, Antonio Pires Da Silva Baptista, and Stefan Uderhardt for critical review of the manuscript. This research was supported by the Intramural Research Program, NIAID, NIH.

1. Ertürk A, et al. (2012) Three-dimensional imaging of solvent-cleared organs using 3DISCO. *Nat Protoc* 7:1983–1995.
2. Renier N, et al. (2014) iDISCO: A simple, rapid method to immunolabel large tissue samples for volume imaging. *Cell* 159:896–910.
3. Hama H, et al. (2015) ScaleS: An optical clearing palette for biological imaging. *Nat Neurosci* 18:1518–1529.
4. Hama H, et al. (2011) Scale: A chemical approach for fluorescence imaging and reconstruction of transparent mouse brain. *Nat Neurosci* 14:1481–1488.
5. Tainaka K, et al. (2014) Whole-body imaging with single-cell resolution by tissue decolorization. *Cell* 159:911–924.
6. Chung K, et al. (2013) Structural and molecular interrogation of intact biological systems. *Nature* 497:332–337.
7. Yang B, et al. (2014) Single-cell phenotyping within transparent intact tissue through whole-body clearing. *Cell* 158:945–958.
8. Murray E, et al. (2015) Simple, scalable proteomic imaging for high-dimensional profiling of intact systems. *Cell* 163:1500–1514.
9. Dodt HU, et al. (2007) Ultramicroscopy: Three-dimensional visualization of neuronal networks in the whole mouse brain. *Nat Methods* 4:331–336.
10. Kuwajima T, et al. (2013) ClearT: A detergent- and solvent-free clearing method for neuronal and non-neuronal tissue. *Development* 140:1364–1368.
11. Ke MT, Fujimoto S, Imai T (2013) SeeDB: A simple and morphology-preserving optical clearing agent for neuronal circuit reconstruction. *Nat Neurosci* 16:1154–1161.
12. Richardson DS, Lichtman JW (2015) Clarifying tissue clearing. *Cell* 162:246–257.
13. Gerner MY, Kastenmuller W, Ifrim I, Kabat J, Germain RN (2012) Histo-cytometry: A method for highly multiplex quantitative tissue imaging analysis applied to dendritic cell subset microanatomy in lymph nodes. *Immunity* 37:364–376.
14. Gerner MY, Torabi-Parizi P, Germain RN (2015) Strategically localized dendritic cells promote rapid T cell responses to lymph-borne particulate antigens. *Immunity* 42:172–185.
15. Fonseca DM, et al. (2015) Microbiota-dependent sequelae of acute infection compromise tissue-specific immunity. *Cell* 163:354–366.
16. Liu Z, et al. (2015) Immune homeostasis enforced by co-localized effector and regulatory T cells. *Nature* 528:225–230.
17. Radtke AJ, et al. (2015) Lymph-node resident CD8α+ dendritic cells capture antigens from migratory malaria sporozoites and induce CD8+ T cell responses. *PLoS Pathog* 11:e1004637.
18. Petrovas C, et al. (2012) CD4 T follicular helper cell dynamics during SIV infection. *J Clin Invest* 122:3281–3294.
19. Torabi-Parizi P, et al. (2014) Pathogen-related differences in the abundance of presented antigen are reflected in CD4+ T cell dynamic behavior and effector function in the lung. *J Immunol* 192:1651–1660.
20. Lee YJ, et al. (2015) Tissue-specific distribution of iNKT cells impacts their cytokine response. *Immunity* 43:566–578.
21. Tsujikawa T, et al. (2017) Quantitative multiplex immunohistochemistry reveals myeloid-inflamed tumor-immune complexity associated with poor prognosis. *Cell Rep* 19:203–217.
22. Steinert EM, et al. (2015) Quantifying memory CD8 T cells reveals regionalization of immunosurveillance. *Cell* 161:737–749.
23. Qi H, Kastenmüller W, Germain RN (2014) Spatiotemporal basis of innate and adaptive immunity in secondary lymphoid tissue. *Annu Rev Cell Dev Biol* 30:141–167.
24. Mueller SN, Germain RN (2009) Stromal cell contributions to the homeostasis and functionality of the immune system. *Nat Rev Immunol* 9:618–629.
25. Gray EE, Cyster JG (2012) Lymph node macrophages. *J Innate Immun* 4:424–436.
26. Kastenmüller W, et al. (2013) Peripheral prepositioning and local CXCL9 chemokine-mediated guidance orchestrate rapid memory CD8+ T cell responses in the lymph node. *Immunity* 38:502–513.
27. Sung JH, et al. (2012) Chemokine guidance of central memory T cells is critical for antiviral recall responses in lymph nodes. *Cell* 150:1249–1263.
28. Woodruff MC, Herndon CN, Heesters BA, Carroll MC (2013) Contextual analysis of immunological response through whole-organ fluorescent imaging. *Lymphat Res Biol* 11:121–127.
29. Ferris AM, Giberson RT, Sanders MA, Day JR (2009) Advanced laboratory techniques for sample processing and immunolabeling using microwave radiation. *J Neurosci Methods* 182:157–164.
30. Mertz J (2011) Optical sectioning microscopy with planar or structured illumination. *Nat Methods* 8:811–819.
31. Amat F, et al. (2015) Efficient processing and analysis of large-scale light-sheet microscopy data. *Nat Protoc* 10:1679–1696.
32. Stegmaier J, et al. (2016) Real-time three-dimensional cell segmentation in large-scale microscopy data of developing embryos. *Dev Cell* 36:225–240.
33. Gerdes MJ, et al. (2013) Highly multiplexed single-cell analysis of formalin-fixed, paraffin-embedded cancer tissue. *Proc Natl Acad Sci USA* 110:11982–11987.
34. Schubert W, et al. (2006) Analyzing proteome topology and function by automated multidimensional fluorescence microscopy. *Nat Biotechnol* 24:1270–1278.

# Supporting Information

## Li et al. 10.1073/pnas.1708981114

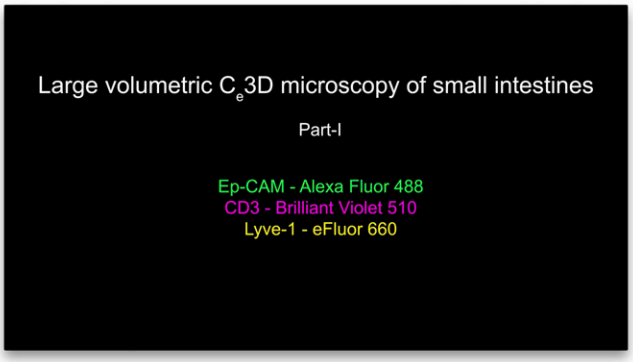


**Movie S1.** Large volumetric $C_e$3D microscopy of small intestines. Small intestines from wild-type (part I) or CD11c-YFP reporter (part II) animals were stained with the indicated antibodies, cleared and imaged via confocal microscopy. Movies demonstrate spatial relationships between the mucosal epithelium (Ep-CAM$^+$), T cells (CD3$^+$), dendritic cells (CD11c-YFP$^+$), and lymphatics (Lyve-1$^+$).

Movie S1

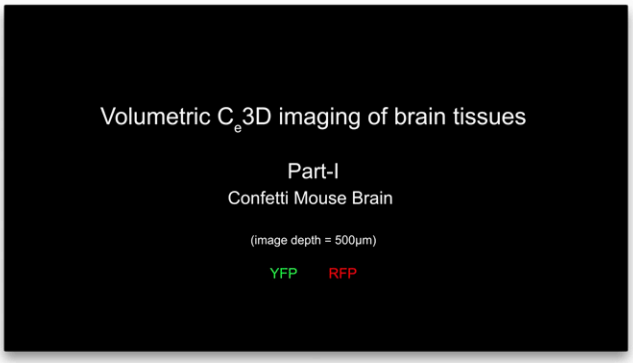


**Movie S2.** Volumetric $C_e$3D imaging of brain tissues. (Part I) $C_e$3D-treated Confetti mouse brain tissues were imaged, with the movie demonstrating individual neuronal cell bodies and axonal processes in the hippocampal and isocortical regions of the cerebral cortex.

Movie S2

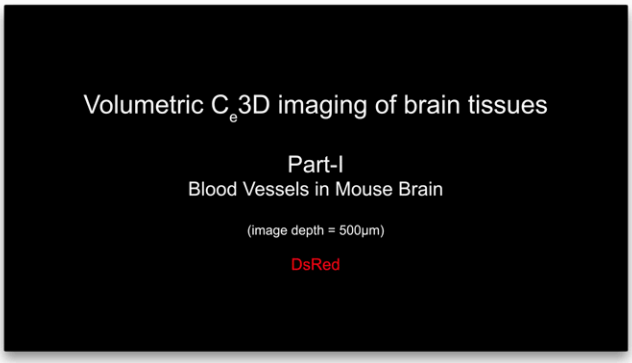


**Movie S3.** Additional volumetric $C_e$3D imaging of brain tissues. (Part I) Cleared brain tissues from actin-DsRed animals allow visualization of the dense blood vascular networks. (Part II) Anti-GFAP antibody stained and cleared Confetti brain tissues allow for simultaneous visualization of astrocytes and neurons.

Movie S3

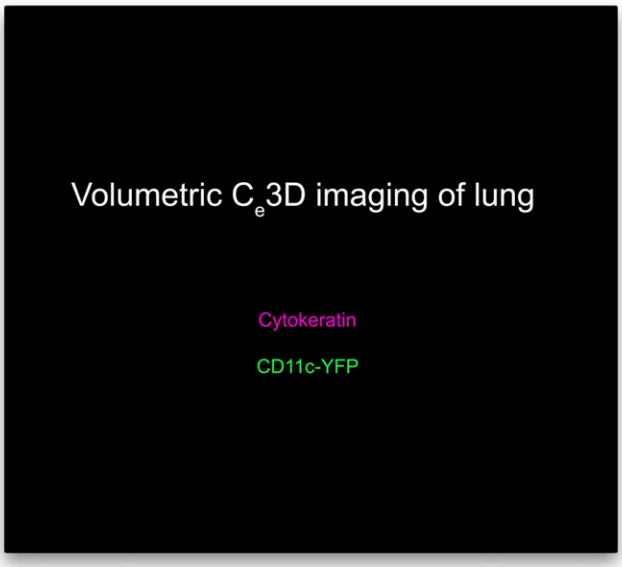


**Movie S4.** Volumetric imaging of CD11c-YFP lungs. Fixed lungs from CD11c-YFP mice were stained with an anti-cytokeratin antibody, $C_e$3D cleared, and imaged via confocal microscopy. Movie demonstrates complex 3D associations between dendritic cells and the bronchial epithelium.

Movie S4

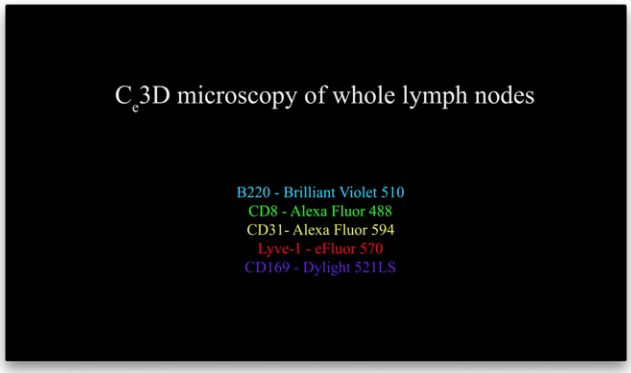


**Movie S5.** C$_e$3D microscopy of whole LNs. Isolated LNs were stained with the indicated antibodies, cleared, and imaged. Movie demonstrates complex branching of the blood vascular networks and spatial organization of various lymphoid and stromal cell populations, and it also highlights the high image quality obtained with the C$_e$3D technique.

Movie S5

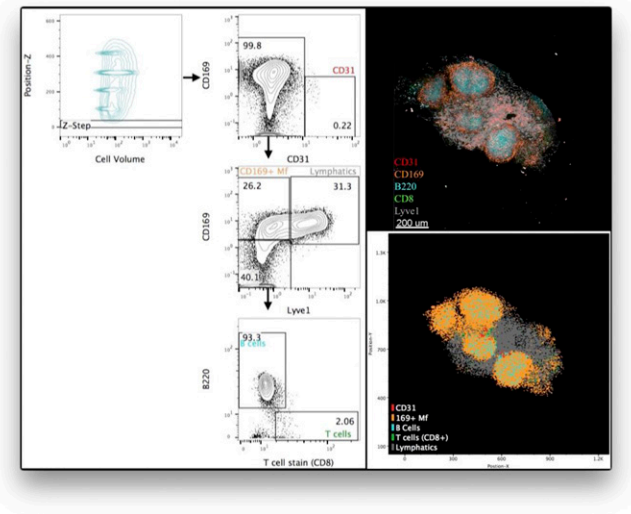


**Movie S6.** C$_e$3D enabled histo-cytometry of whole LNs. Statistical information on all segmented cell objects from imaged LNs was imported into FlowJo software. Cellular position in the Z dimension was next used to create a Z-step gate (*Left*), with the gated cells further analyzed for phenotypic marker expression (*Middle*). All gated cells, denoted by the indicated colors, were next plotted on a X by Y positional plot (*Bottom Right*), with the original imaged tissue in the corresponding Z volume also displayed (*Top Right*) for direct comparison.

Movie S6

## Other Supporting Information Files

SI Appendix (PDF)

# SUPPORTING INFORMATION APPENDIX

**Multiplex, quantitative cellular analysis in large tissue volumes with Clearing-enhanced 3D microscopy ($C_e$3D)**

Weizhe Li, Ronald N. Germain and Michael Y. Gerner

**CONTENTS:**

## SUPPLEMENTARY METHODS

### Tissue isolation and fixation

LNs were harvested and fixed with 0.05 M phosphate buffer containing 0.1 M L-lysine (pH 7.4), 2 mg/ml NaIO4 and 1 percent PFA overnight at 4 Celsius. For non-LN tissues with significant erythrocytic composition (kidney, liver, etc…), cardiac perfusion was first performed with 1X PBS, followed by 4 percent PFA in PBS. For brain tissues, BD Fixation buffer was used for initial perfusion fixation, with the organ next cut via vibratome into individual 1-2mm slices, which were further fixed using 1:4 PBS diluted BD Cytofix/Cytoperm buffer (BD Biosciences) at 4 degrees overnight.

### Whole Mount Staining

Fixed tissues were incubated for at least 8 hours in a blocking buffer containing 1% normal mouse serum, 1% bovine serum albumin and 0.3% Triton X-100. For brain slices, BD Permeabilization buffer (BD Biosciences), supplemented with 1% normal mouse serum and bovine serum albumin, was used to block and permeabilize tissues for up to 3 days at 37 degrees Celsius. Tissues were next incubated with directly conjugated antibodies, diluted 1:100 in the blocking buffer, for 3 days at 24 or 37 degrees Celsius on a shaker, with higher temperatures allowing for more rapid tissue staining. Large molecular weight fluorophores, such as allophycocyanin, R-phycoerythrin and brilliant violet polymers were avoided, as these exhibited slow tissue penetration and often resulted in nonhomogeneous staining. Stained samples were washed with PBS containing 0.2% Triton-X100 and 1-thioglycerol (0.5%) for 12-24 hours at 24 or 37 degrees Celsius. Brain tissues were washed with the BD Permeabilization buffer (BD Biosciences).

### $C_e$3D Tissue Clearing

Stock N-methylacetamide (Sigma) was prepared by diluting melted N-methylacetamide to 40% (v/v) in PBS, which was then used to dissolve Histodenz (Sigma) to 86% (w/v) concentration [~1.455g Histodenz per 1ml 40% N-methylacetamide] inside a chemical fume hood, with the mixture incubated at 37 degrees Celsius to expedite dissolution time. Triton X-100 (0.1% v/v) and 1-thioglycerol (0.5% v/v) were added to the clearing solution. The final $C_e$3D medium refractive index can range between 1.49 and 1.5. Stained and washed tissues were placed in the $C_e$3D medium inside a chemical fume hood and incubated at room temperature on a rotor for 12-72 hours. Total incubation time depended on tissue size, with the clearing medium replaced once during the incubation for larger tissue samples.

## $C_e$3D Imaging

Stained and cleared tissues were embedded in fresh $C_e$3D medium within a vacuum grease or silicone gel spacer either on a microscope slide or in a glass-bottom 35mm dish and tightly covered with a cover glass. Confocal imaging was performed on an inverted SP8 microscope (Leica Microsystems) using either a 20x 0.75NA 670um working distance or a 40x 1.3NA 240um working distance objective. 512x512 or 1024x1024 voxel density at 1-1.5x optical zoom was used, with the voxel size ranging from 0.3-0.6um in the lateral and 0.5-1.0um in the axial directions. To achieve larger working distances, certain experiments utilized the 25X 1.0NA motCORR objective from Leica, with the samples illuminated using two-photon excitation on an upright SP8.

## Quantitative comparison of uncleared and $C_e$3D samples

For studies comparing tissue sections before and after $C_e$3D treatment, fixed tissues were washed 3 times for 20 min in 0.05 M phosphate buffer, embedded in 2 percent low melting agarose and cut into 200um sections with a vibratome. Individual sections were next blocked with a blocking buffer containing 1% normal mouse serum, 1% bovine serum albumin and 0.3% Triton X-100, then stained with directly labeled antibodies at 37 degrees Celsius overnight on a shaker. Stained tissues were then embedded in PBS on a microscope slide, coverslipped and imaged with a confocal microscope. Next, tissues were cleared with $C_e$3D, re-embedded on slides and re-imaged. Matched tissue areas were then identified in Imaris, with individual cells next compared for retaining reporter and antibody-based fluorescence before and after clearing.

## $C_e$3D Cell Segmentation Pipeline:

Collected images were corrected for fluorophore spillover using the Leica Channel Dye Separation Module, deconvolved via Huygen's Essential software (Scientific Volume Imaging) and imported into Imaris (Bitplane Scientific Software). Images were next converted into 8-bit format and corrected for z attenuation using the Attenuation Correction extension in Imaris. The Linear Stretch plugin was used to normalize channel histograms. All channels representing membrane surface stains were next summed into a new Sum Channel using Channel Arithmetics. Since different surface markers vary in brightness relative to one another, correction factors (multipliers) were used during this summation step to optimize the overall homogeneity of the Sum Channel across the imaged tissue. Similar correction was performed to normalize the Sum Channel for cells defined by one vs. multiple markers. This resultant Sum Channel was then exported into FIJI (ImageJ) for

further processing. In FIJI, the Sum Channel was first inverted to create an Inverse Sum Channel. Improved contrast and cell separation was observed by further subtracting the Sum Channel from the Inverse Sum Channel, which was then used for further processing. Next, the Inverse Sum Channel was used to create 2D skeletons in the XY, XZ and YZ planes. For this, the Inverse Sum Channel was rotated 90 degrees along the X and Y axes using the Transform-J FIJI plugin. The images were then binarized using the Median Auto Local Thresholding tool and despeckled using the Despeckle plugin in order to remove noise and minimize improper generation of skeleton lines. The images were next processed via the 2D Skeleton plugin, inverted to create a white skeleton signal and rotated back to the original views using the Transform-J function. The XY, XZ and YZ skeletons were next subtracted from the Inverse Sum Channel to improve cellular separation in 3D space. This new calculated channel was then imported back into the original image in Imaris. Here, the Gamma Correction plugin was used on the calculated channel to enhance signal variation from the center to the edges of individual cells. Finally, either the Surface Creation or Cell Creation module in Imaris was used to segment individual cell objects within the image, with the statistics for all segmented cells exported as individual comma separated value (CSV) files. Mean Channel Intensity, Volume, Sphericity, Position, as well as Object Identifier statistics were compiled into a single CSV matrix file and imported into Flowjo software (Treestar Inc.) for final hierarchical gating analysis.

**Computational Specifications**

For cell segmentation and data processing, we recommend a high speed 8-12 core processor, large amounts of RAM (>128GB), PCIe SSD hard drive for fast read/write capacity, and at least an 8GB VRAM graphics card. For long term storage of data, we recommend using USB-3 or USB-C large capacity portable drives. Recent changes in Imaris software architecture have dramatically improved the Surface creation module, which currently outperforms the Cell module with respect to computational speed.

**Non-$C_e$3D clearing methods**

<u>3DISCO</u>

For 3DISCO clearing [1], antibody stained samples were incubated in graded steps of 50%, 70%, 80% Tetrahydrofuran in $dH_20$ for 20min each, followed by three 20 minute treatments with 100% Tetrahydrofuran. Next, samples were placed in Dichloromethane for 15-30min, and finally placed in di-benzyl ether until cleared.

<u>CUBIC</u>

For CUBIC clearing [2], samples were first placed into ScaleCUBIC-1 solution and incubated at 37 degree overnight. Samples were next washed in PBS, blocked and

stained with directly conjugated antibodies. Finally, samples were incubated by ScaleCUBIC2 solution overnight at room temperature, until cleared.

PACT

For PACT clearing [3], samples were placed inside a 15ml conical tube with 15ml A4P0 solution and incubated at 4 degrees Celsius overnight. A4P4 solution was also tried, but some antibodies displayed reduced staining as compared to the A4P0 solution. The sample tube was evacuated in vacuum and then bubbled with nitrogen gas for 5min. The samples were next placed into an incubator at 37 degrees Celsius for approximately 4 hours, until all liquid was polymerized. After extraction from polymerized gel, samples were placed in a 8% SDS solution and incubated overnight at 37 degree Celsius on a shaker. After thoroughly washing with PBS to get rid of SDS, samples were next stained with directly conjugated antibodies and washed. Finally, partially cleared samples were placed in the RIMS solution for final clearing.

AbSca*l*e

For AbSca*l*e clearing [4], fixed and washed lymph nodes were treated with Sca*l*eS0 solution (containing 20% sorbitol, 5% glycerol, 1 mM methyl-β-cyclodextrin, 1 mM γ-cyclodextrin, 1% N-acetyl-L-hydroxyproline, and 3% DMSO) overnight at 37 degrees Celsius. Samples were next treated with Sca*l*eA2 solution (10% Glycerol, 4M Urea, 0.1% Triton X-100) for 24 hours at 37 degrees Celcius. Next, samples were incubated in ScaleB4(0) solution (including 8M Urea) for 12 hours at 37 degrees Celsius. Samples were then treated by Sca*l*eA2 again for 12 hours at 37 degrees, and next washed in PBS for 6 hours at room temperature. Direct antibody staining was performed in AbSca*l*e solution (PBS(–) solution containing 0.33 M urea, 0.1–0.5% Triton X-100) overnight at 37 degrees Celsius with agitation. Stained samples were next washed with the AbSca*l*e solution for 6 hours, followed by a AbSca*l*e rinse ( 0.1× PBS(–) solution containing 2.5% BSA, 0.05% (w/v) Tween-20) for 2 hours at room temperature. Re-fixation was next performed using 4% PFA/PBS for 1 hour at room temperature, followed with a PBS wash step. Finally, clearing was performed using the Sca*l*eS4 solution (40% Sorbitol, 10% Glycerol, 4M Urea, 0.2% Triton X-100, 20% DMSO) for 12 hours at 37 degrees Celsius.

*Clear*$^{T/T2}$

For *Clear*$^{T}$ clearing [5], fixed, stained and washed lymph nodes were incubated sequentially in 20% for 15 minutes, 40% for 15 minutes, 80% for 15 minutes, 95% for 15 minutes, and 95% formamide for 30 minutes at room temperature. For the comparison of uncleared and *Clear*$^{T}$ cleared samples, 200 um sections were used. Samples were incubated 5 minutes in 20%, 40%, 80%, 95% formamide, and then in 95% formamide for 15 minutes.

For *Clear*$^{T2}$ clearing [5], fixed, stained and washed lymph nodes were incubated sequentially in 25% formamide/10% PEG for 30 minutes, 50% formamide/20%

PEG for 15 minutes, and 50% formamide/20% PEG for 1 hour at room temperature. For the comparison of uncleared and *Clear$^{T2}$* cleared samples, 200 um sections were used. Samples were incubated 10 minutes in 25% formamide/10% PEG, and then incubated in 5 minutes in 50% formamide/20% PEG, and in 50% formamide/20% PEG for 30 minutes.

SeeDB

For SeeDB clearing [6], fixed, stained and washed lymph nodes were incubated sequentially in 20%, 40%, 60%, 80%, and 100% (w/v) d(−)-fructose solutions for 1hour, 1hour, 1hour, 1hour, 2hours, and 2hours, respectively, at room temperature. The samples were next incubated in SeeDB solution for 24 hours.

iDISCO/iDISCO+

For iDISCO clearing [7], fixed samples (200 µm sections) were washed in PBS for 1 hour twice and pretreated according to protocol without methanol. Tissues were then incubated in PBS/0.2% Triton X-100/20% DMSO/0.3 M glycine at 37°C overnight. Samples were next blocked in PBS/0.2% Triton X-100/10% DMSO/6% Donkey Serum at 37°C for 4 hours, and then washed twice for 1hr in PBS/0.2% Tween-20 with 10 µg/ml heparin (PTwH). Antibodies were diluted in PTwH/5% DMSO/3% Donkey Serum. Samples were stained at 37°C overnight in the antibody mix and then washed twice in PTwH for 2 hours. Samples were next cleared by incubation in 50%, 80% Tetrahydrofuran in $dH_20$ for 20min each, followed by three 20 minute treatments with 100% Tetrahydrofuran. Next, samples were placed in Dichloromethane for 15-30min, and finally placed in di-benzyl ether until cleared.

For iDISCO+ clearing [8], fixed samples (200 µm sections) were washed in PBS for 1 hour twice and pretreated in 20%, 40%, 60%, 80%, 100%, 100% methanol (in $ddH_2O$) solutions for 1 hour each at room temperature. Samples were then bleached using 5% $H_2O_2$ at 4 degrees overnight. Next, samples were re-hydrated in 80%, 60%, 40%, 20%, and $H_2O$ steps for 1 hour at room temperature, and then pretreated in PBS / 0.2% TritonX-100 / 20% DMSO / 0.3M glycine at 37°C overnight. Tissues were then blocked in PBS / 0.2% TritonX-100 / 10% DMSO / 6% Donkey Serum at 37°C for 1 day, then incubated with antibodies in PBS-Tween 0.2% with Heparin 10µg/mL (PTwH) / 5% DMSO / 3% Donkey Serum at 37°C overnight, and then washed twice in PTwH for 2 hours. After staining, samples were dehydrated in 20%, 40%, 60%, 80%, 100%, 100% methanol (in $ddH_2O$) steps for 1 hour at room temperature. After overnight incubation in Methanol/Dichloromethane (1:2 v/v), samples were washed twice in Dichloromethane for 20min. At last, samples were placed in di-benzyl ether until cleared.

**SUPPLEMENTARY REFERENCES**


1. Erturk, A. et al. Three-dimensional imaging of solvent-cleared organs using 3DISCO. *Nature protocols* **7**, 1983-1995 (2012).
2. Susaki, E.A. et al. Whole-brain imaging with single-cell resolution using chemical cocktails and computational analysis. *Cell* **157**, 726-739 (2014).
3. Treweek, J.B. et al. Whole-body tissue stabilization and selective extractions via tissue-hydrogel hybrids for high-resolution intact circuit mapping and phenotyping. *Nature protocols* **10**, 1860-1896 (2015).
4. Hama, H. et al. Sca/eS: an optical clearing palette for biological imaging. *Nat Neurosci* **18**, 1518-+ (2015).
5. Kuwajima, T. et al. ClearT: a detergent- and solvent-free clearing method for neuronal and non-neuronal tissue. *Development* **140**, 1364-1368 (2013).
6. Ke, M.T. & Imai, T. Optical clearing of fixed brain samples using SeeDB. *Current protocols in neuroscience / editorial board, Jacqueline N. Crawley ... [et al.]* **66**, Unit 2 22 (2014).
7. Renier, N., et al., iDISCO: a simple, rapid method to immunolabel large tissue samples for volume imaging. *Cell*, **159**, 896-910 (2014).
8. Renier N, et al., Mapping of Brain Activity by Automated Volume Analysis of Immediate Early Genes. *Cell* **165**, 1789–1802 (2016).

**SUPPLEMENTARY FIGURE LEGENDS**

**Supplementary Figure 1**. Comparison of various clearing methods with $C_e$3D for preservation of reporter protein fluorescence and capacity for immunolabeling.
(A) 200um thick sections from CD11c-YFP LN were treated with the indicated published clearing protocols and compared to $C_e$3D clearing or uncleared control samples for preservation of reporter protein fluorescence, as well as the capacity to immunolabel tissues with the indicated fluorophore-conjugated antibodies. Only the first 30um of the section were imaged for direct comparison to uncleared tissues. (B) Mean fluorescence intensity for cells stained with the indicated antibodies or expressing YFP was quantified.

**Supplementary Figure 2**. Additional comparison of published clearing methods.
(A) CD11c-YFP LN were cleared with Clear*T* and Clear*T2* methodologies and compared for relative tissue transparency. (B) 200um thick LN sections treated with Clear*T* and Clear*T2* were compared to uncleared PBS-treated control samples for preservation of reporter protein fluorescence, as well as the capacity to immunolabel tissues with the indicated fluorophore-conjugated antibodies. Only the first 30um of the section were imaged for direct comparison to control tissues. (C) CUBIC treated CD11c-YFP LN were stained with an unconjugated B220 antibody, followed by a goat anti-rat Alexa 594 secondary antibody.

**Supplementary Figure 3**. High-resolution, volumetric imaging of CD11-YFP LN after $C_e$3D clearing. (A) LN from CD11c-YFP mice were stained with the indicated antibodies, cleared with $C_e$3D and imaged by confocal microscopy (top), with individual axial imaging planes examined for uniformity of fluorescence (bottom).

**Supplementary Figure 4**. $C_e$3D optimally preserves cellular morphology.
(A) Kidneys from CD11c-YFP x Actin-DsRed cross animals were compared before and after $C_e$3D treatment (left) and imaged via confocal microscopy (right). (B) Tissue volume after $C_e$3D treatment, as normalized to the starting volume. (C) Thick brain slices were stained with anti-GFAP antibody to label astrocytes and cleared with the indicated methods. Astrocytes were next imaged in similar brain regions, and the preservation of cellular morphological processes was compared to uncleared control tissues, with tissue sections used for direct comparison (top). Astrocyte sphericity and GFAP-staining intensity was quantified. Each symbol represents an individual cell within an image (bottom). (D) GFP expressing neurons from Confetti reporter brain tissues were imaged (left) and examined for changes in cell size and sphericity (right). (E) CD11c-YFP expressing dendritic cells in LNs and small intestines were imaged (left) and quantified for average cellular volume and cellular complexity, as measured by object sphericity (right). Tissue sections were used to allow direct comparison to uncleared control samples.

**Supplementary Figure 5**. $C_e$3D preserves reporter protein and antibody-based fluorescence. (A) Confetti reporter mouse tissues were examined for fluorescence of GFP, YFP, RFP and CFP reporter proteins with or without $C_e$3D treatment (top). Due to organ-specific expression of fluorescent proteins, CFP image was taken in a separate site. Mean reporter fluorescence intensity (MFI) for reporter expressing cells was quantified (bottom). (B) CD11c-YFP LN sections were stained with the indicated antibodies and imaged before and after treatment with $C_e$3D. Average cellular reporter and antibody-based fluorescence were quantified (bottom).

**Supplementary Figure 6**. $C_e$3D enables large volumetric imaging of various tissues with preservation of cellular morphology. Large volumetric scans of cleared tissues are presented (left), with zoom-in virtual sections (right) demonstrating cellular morphology and quality of reporter and antibody-based fluorescence. (A) Isolated segments from the small intestines of CD11c-YFP mice were stained with the indicated antibodies, cleared and imaged. (B) 1mm brain slices stained with anti-GFAP antibody demonstrates astrocyte cellular projections. (C) Cx3cr1-GFP brain tissues allow visualization of the branching patterns of ramified microglial cells. Cleared (D) lung, (E) thymus and (F) liver tissues from CD11c-YFP animals demonstrate dendritic cell processes and associations with various anatomical structures. Liver autofluorescence (AF, cyan) is also presented to demonstrate the relationships between Kupffer cells and liver sinusoids.

**Supplementary Figure 7**. $C_e$3D multiplex imaging and high-resolution quantitative Histo-Cytometry. (A) Same LN as in Main Figure 4A is presented in a rotated orientation, with the individual stains isolated as separate channels. 3D cross-section zoom-in view demonstrates relatively high quality of imaging, but with some spatial overlap between signals from Lyve-1 expressing lymphatic vessels (white) and CD169 expressing medullary macrophages (orange). (B) Cell membrane signals were used to create cell objects and exported for analysis in FlowJo, as presented in Main Figure 4. (C) LN were stained with the CD169 and Lyve-1 antibodies, cleared and imaged with a 40x 1.3NA objective. (D) Images were next segmented with cell statistics exported into FlowJo for (D) quantitative population gating and positional analysis.

**Supplementary Figure 8**. Multiplex panel for quantitative $C_e$3D Histo-Cytometry of lymphocyte populations. Maximum projection images of the individual acquired channels for the merged LN image presented in Main Figure 5A. Zoom-in view of a maximum projection for a 20um-thick virtual slice demonstrates an area enriched in $CD25^+$ cell clusters (arrows).

**Supplementary Figure 9**. High-resolution, large volumetric imaging of $C_e$3D treated tissues. Lungs were labeled with Alexa 647 conjugated anti-cytokeratin antibody and cleared with $C_e$3D. (A) Tissues were imaged from the anterior to posterior surfaces using the 25x 1.0NA motCORR objective with a step size of 5um and two-photon excitation. Total imaged depth was 3mm. (B) Various virtual optical sections along the imaged volume are presented, with the zoom-in panels demonstrating image quality obtained at the different depths.

**Supplementary Figure 10**. $C_e$3D pipeline for tissue clearing, imaging and quantitative Histo-Cytometry. (1) Tissues are fixed, (2) stained with various fluorophore-conjugated antibodies, (3) cleared and (4) imaged. (5) Spectral unmixing to compensate for fluorophore spillover into neighboring detectors is performed. (6) Deconvolution is performed to improve image quality and quantitative accuracy. (7) Images are segmented into individual cell objects, with the objects' statistics then exported into graphing software for (8) population phenotypic gating and (9) quantitative image Histo-Cytometry.

## SUPPLEMENTARY TABLE LEGENDS

**Table 1**. Comparison of the various tested tissue-clearing methods with $C_e$3D. Different parameters desirable for imaging of cleared tissues were compared based on previously published results (P) and empirical observations during direct testing (T).

**Table 2**. Various reagents tested for overall tissue clarification, conservation of reporter protein fluorescence, preservation of antibody-based staining, overall signal quality and morphological integrity. Main $C_e$3D clearing reagent combined with Histodenz is highlighted in red.

**Table 3**. Tested antibodies (left) and fluorophores (right) that were found compatible with $C_e$3D treated tissues. No incompatible probes were seen among all tested reagents. Large molecular weight (MW) probes that require extended incubation times for tissue penetration, or dyes prone to photobleaching over extended imaging depths are indicated.

# Supplementary Figure 1

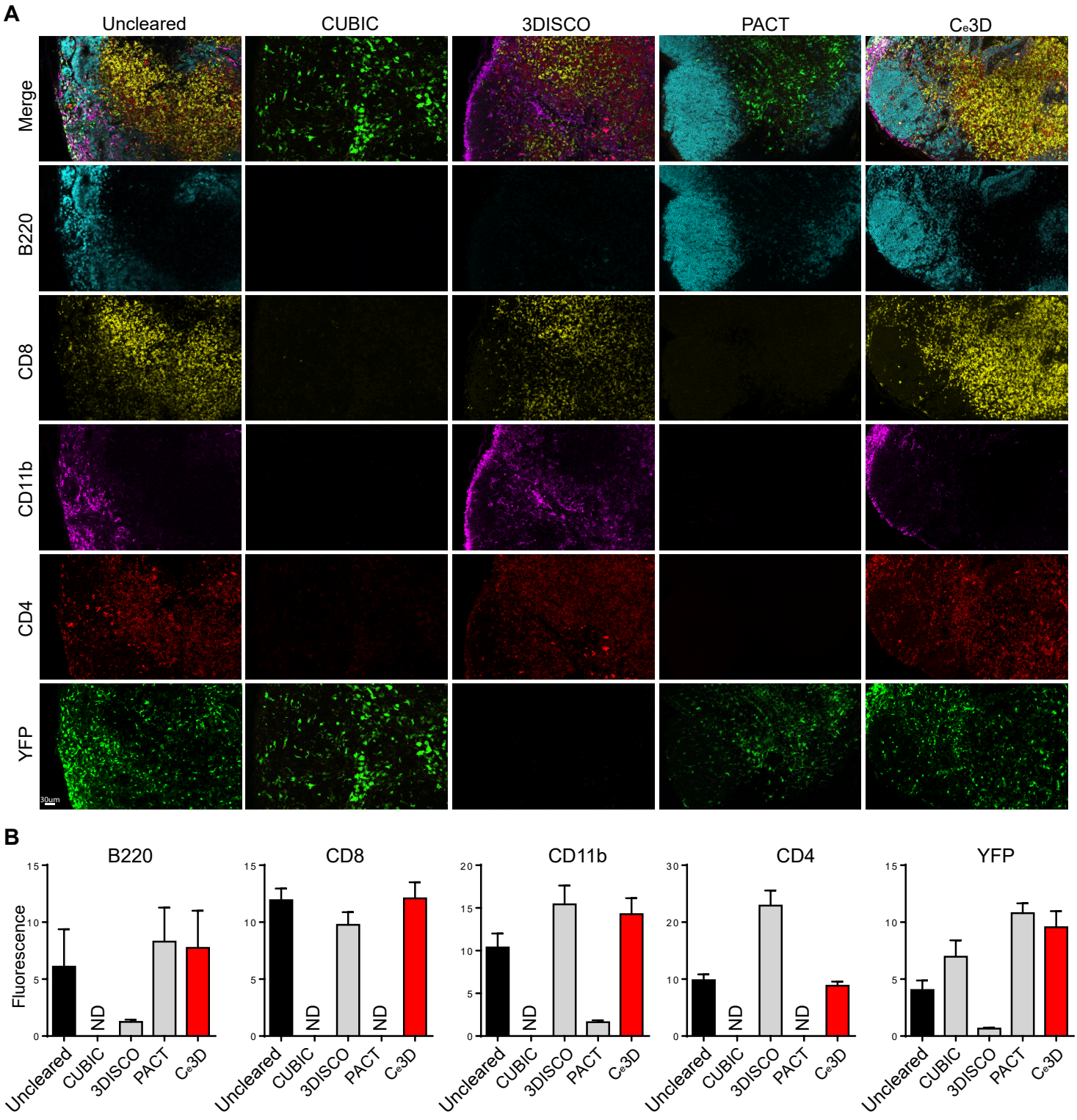


**Figure S1**. Comparison of various clearing methods with $C_e$3D for preservation of reporter protein fluorescence and capacity for immunolabeling.
(A) 200um thick sections from CD11c-YFP LN were treated with the indicated published clearing protocols and compared to $C_e$3D clearing or uncleared control samples for preservation of reporter protein fluorescence, as well as the capacity to immunolabel tissues with the indicated fluorophore-conjugated antibodies. Only the first 30um of the section were imaged for direct comparison to uncleared tissues. (B) Mean fluorescence intensity for cells stained with the indicated antibodies or expressing YFP was quantified.

# Supplementary Figure 2

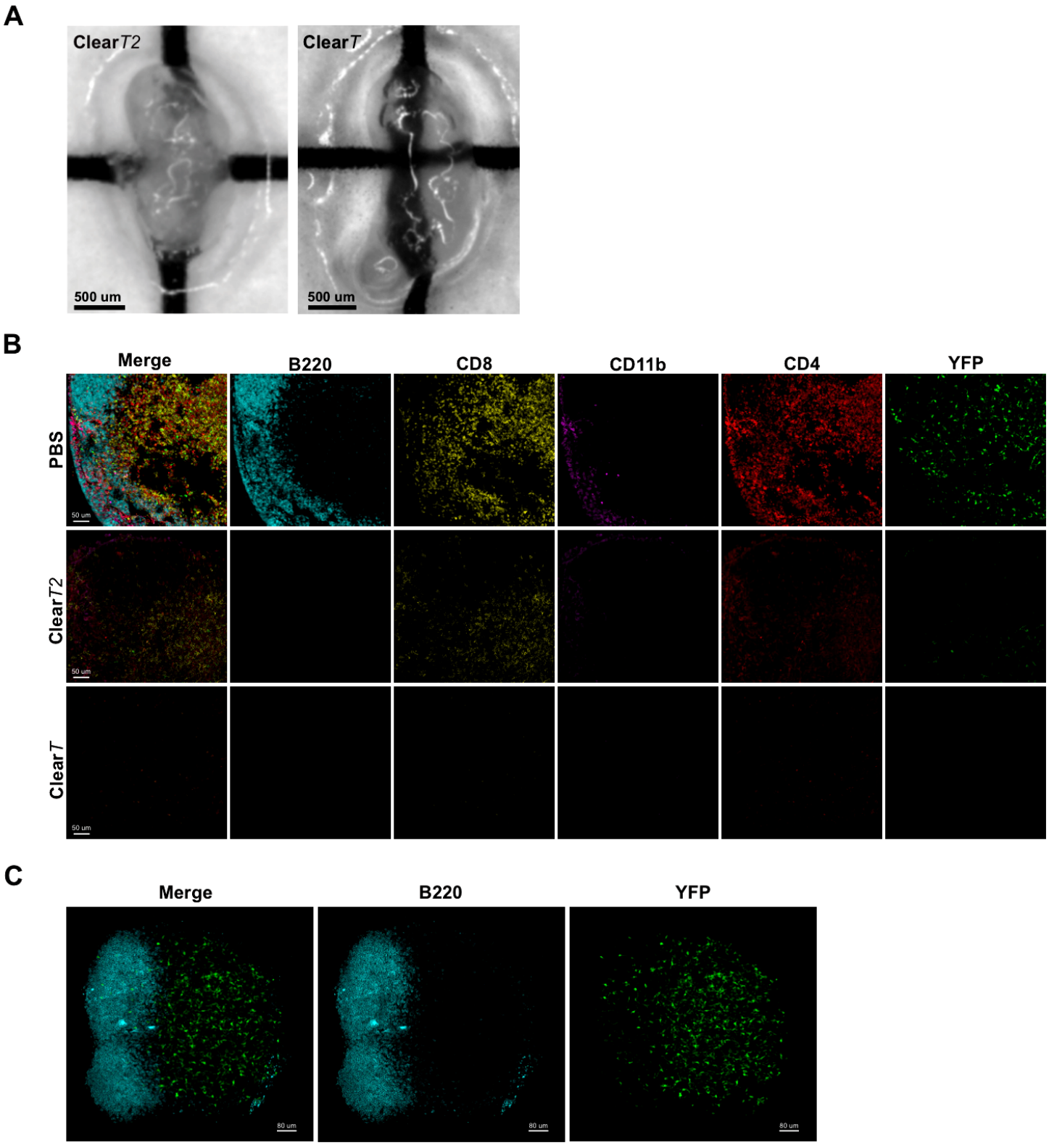


**Figure S2**. Additional comparison of published clearing methods.
(A) CD11c-YFP LN were cleared with Clear*T* and Clear*T2* methodologies and compared for relative tissue transparency. (B) 200um thick LN sections treated with Clear*T* and Clear*T2* were compared to uncleared PBS-treated control samples for preservation of reporter protein fluorescence, as well as the capacity to immunolabel tissues with the indicated fluorophore-conjugated antibodies. Only the first 30um of the section were imaged for direct comparison to control tissues. (C) CUBIC treated CD11c-YFP LN were stained with an unconjugated B220 antibody, followed by a goat anti-rat Alexa 594 secondary antibody.

# Supplementary Figure 3

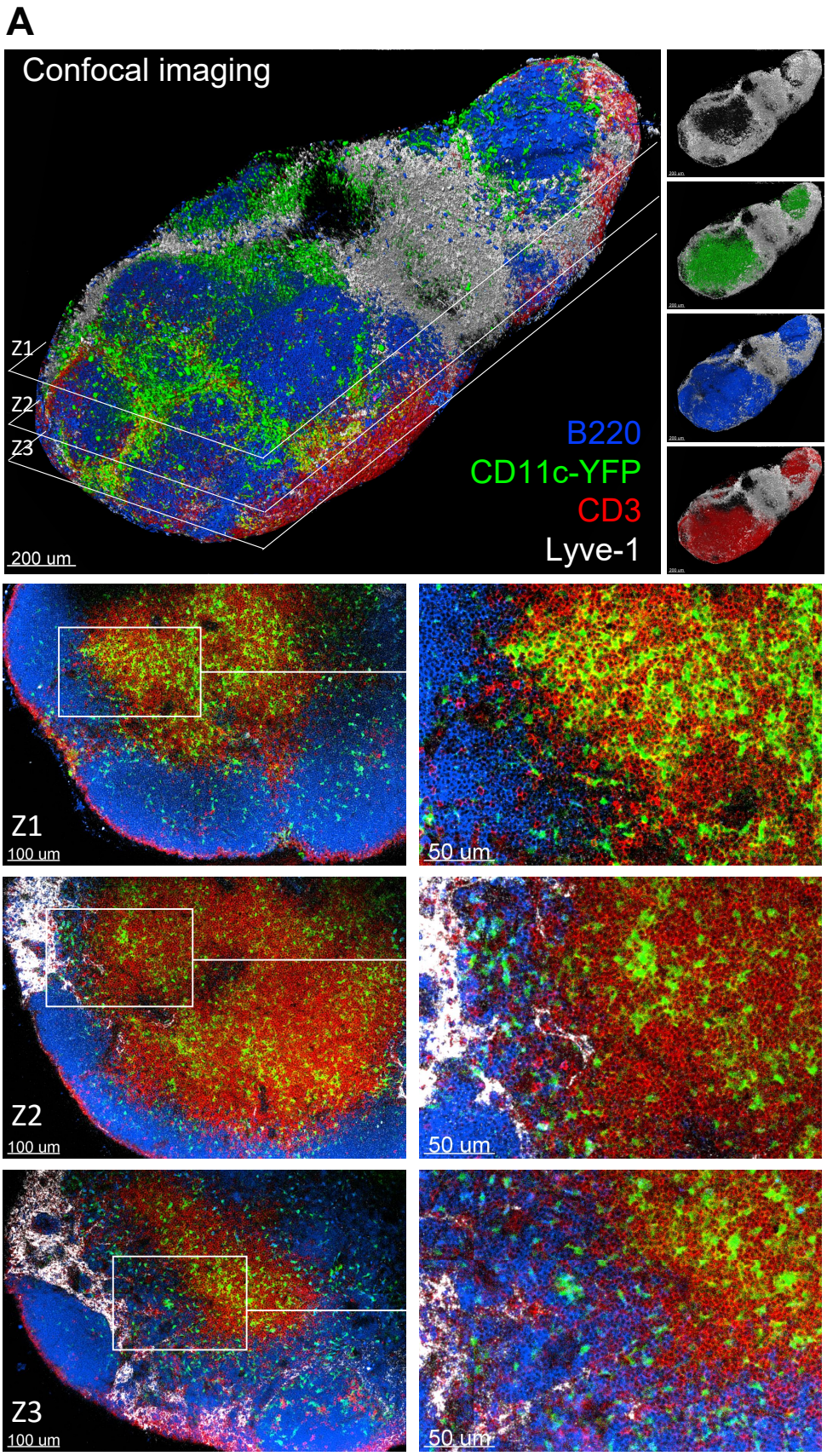


**Figure S3.** High-resolution, volumetric imaging of CD11-YFP LN after $C_e$3D clearing. (A) LN from CD11c-YFP mice were stained with the indicated antibodies, cleared with $C_e$3D and imaged by confocal microscopy (top), with individual axial imaging planes examined for uniformity of fluorescence (bottom).

# Supplementary Figure 4

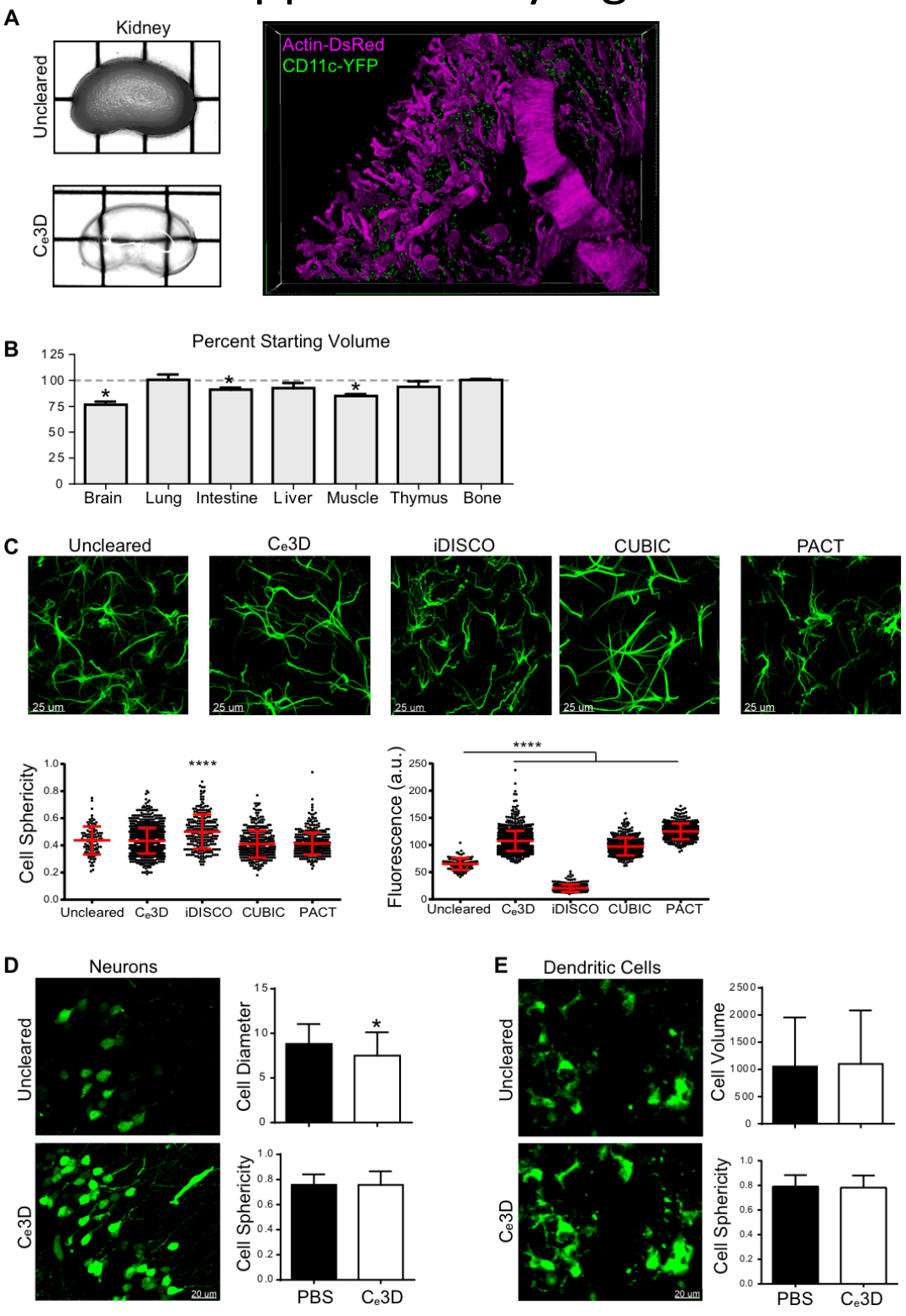


**Figure S4.** $C_e$3D optimally preserves cellular morphology.

(A) Kidneys from CD11c-YFP x Actin-DsRed cross animals were compared before and after $C_e$3D treatment (left) and imaged via confocal microscopy (right). (B) Tissue volume after $C_e$3D treatment, as normalized to the starting volume. (C) Thick brain slices were stained with anti-GFAP antibody to label astrocytes and cleared with the indicated methods. Astrocytes were next imaged in similar brain regions, and the preservation of cellular morphological processes was compared to uncleared control tissues, with tissue sections used for direct comparison (top). Astrocyte sphericity and GFAP-staining intensity was quantified. Each symbol represents an individual cell within an image (bottom). (D) GFP expressing neurons from Confetti reporter brain tissues were imaged (left) and examined for changes in cell size and sphericity (right). (E) CD11c-YFP expressing dendritic cells in LNs and small intestines were imaged (left) and quantified for average cellular volume and cellular complexity, as measured by object sphericity (right). Tissue sections were used to allow direct comparison to uncleared control samples.

# Supplementary Figure 5

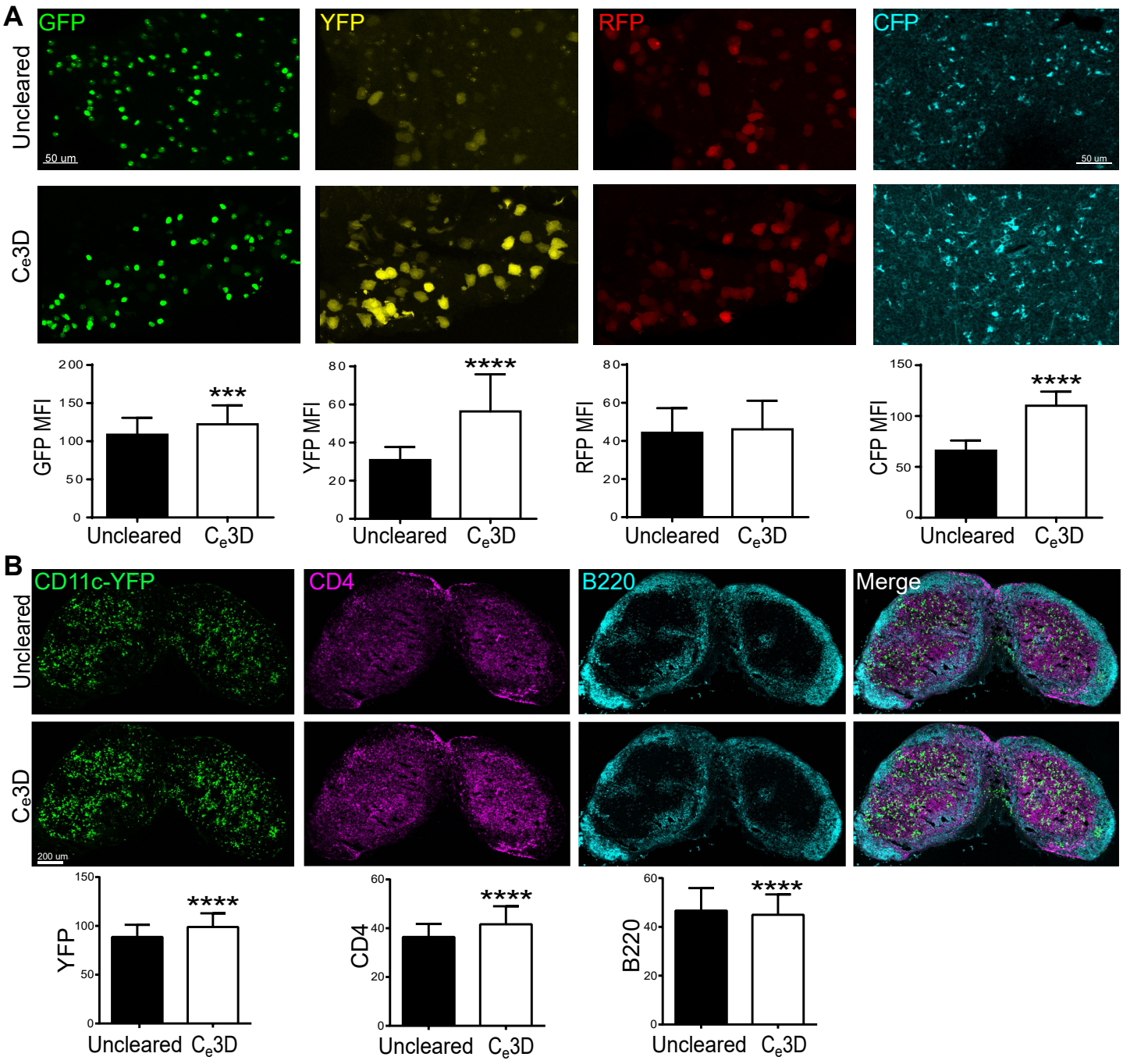


**Figure S5**. $C_e$3D preserves reporter protein and antibody-based fluorescence.
(A) Confetti reporter mouse tissues were examined for fluorescence of GFP, YFP, RFP and CFP reporter proteins with or without $C_e$3D treatment (top). Due to organ-specific expression of fluorescent proteins, CFP image was taken in a separate site. Mean reporter fluorescence intensity (MFI) for reporter expressing cells was quantified (bottom). (B) CD11c-YFP LN sections were stained with the indicated antibodies and imaged before and after treatment with Ce3D. Average cellular reporter and antibody-based fluorescence were quantified (bottom).

# Supplementary Figure 6

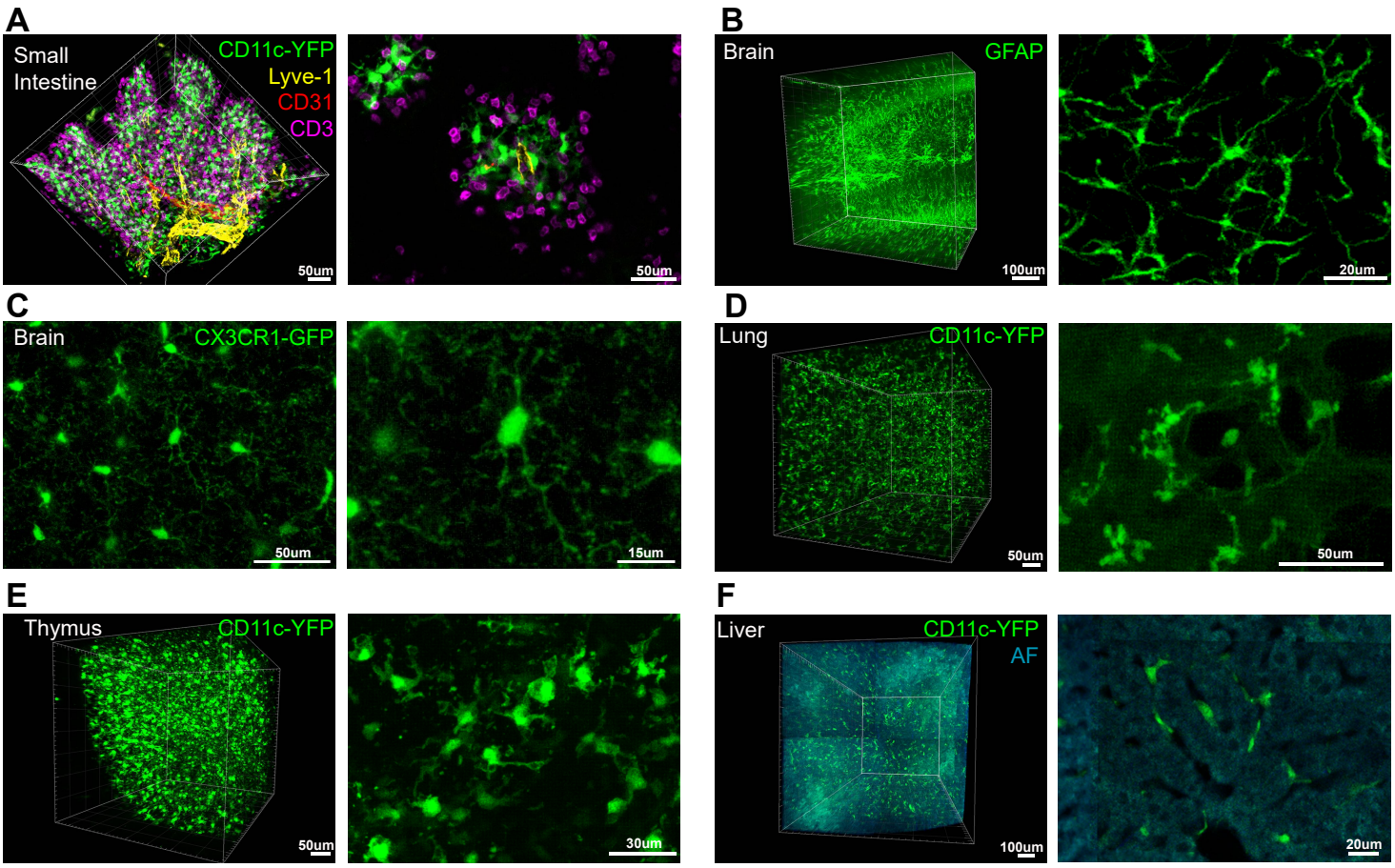


**Figure S6**. $C_e$3D enables large volumetric imaging of various tissues with preservation of cellular morphology.

Large volumetric scans of cleared tissues are presented (left), with zoom-in virtual sections (right) demonstrating cellular morphology and quality of reporter and antibody-based fluorescence. (A) Isolated segments from the small intestines of CD11c-YFP mice were stained with the indicated antibodies, cleared and imaged. (B) 1mm brain slices stained with anti-GFAP antibody demonstrates astrocyte cellular projections. (C) Cx3cr1-GFP brain tissues allow visualization of the branching patterns of ramified microglial cells. Cleared (D) lung, (E) thymus and (F) liver tissues from CD11c-YFP animals demonstrate dendritic cell processes and associations with various anatomical structures. Liver autofluorescence (AF, cyan) is also presented to demonstrate the relationships between Kupffer cells and liver sinusoids.

# Supplementary Figure 7

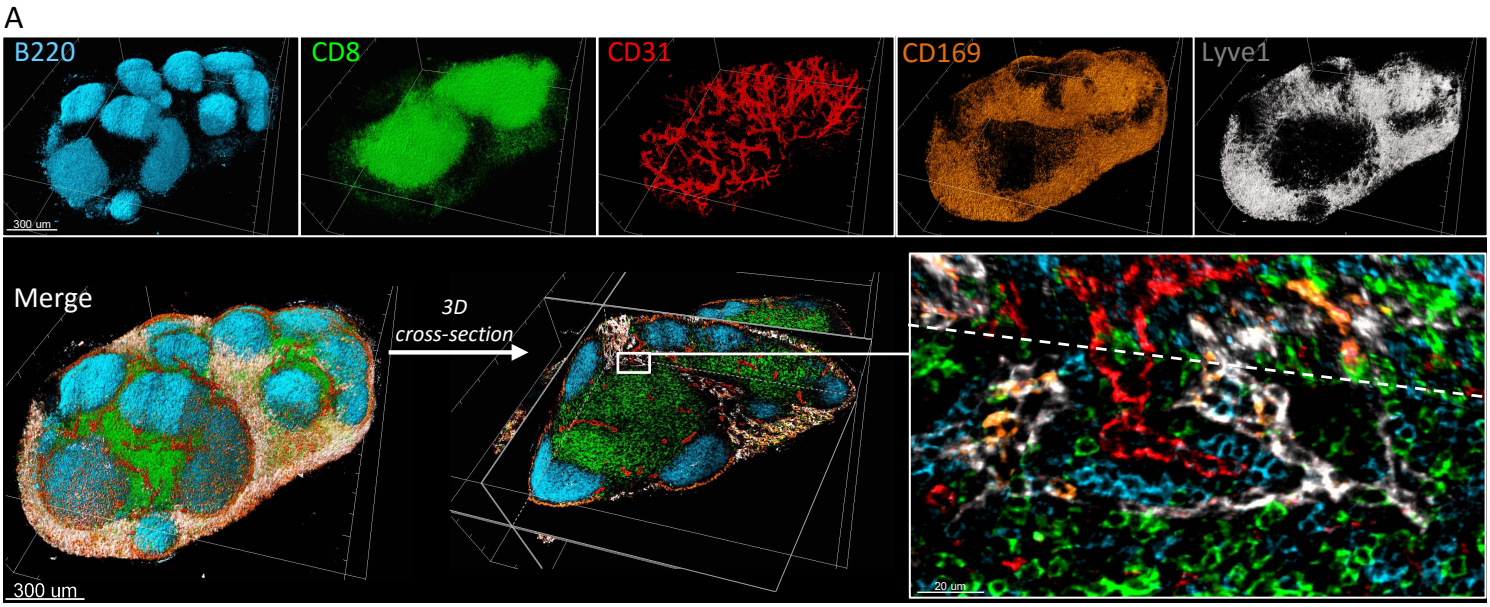


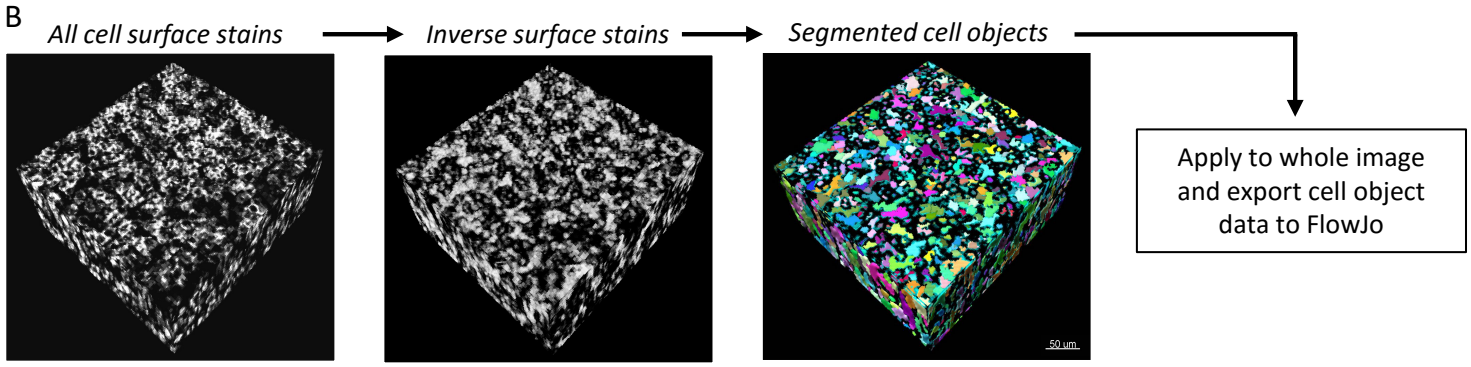


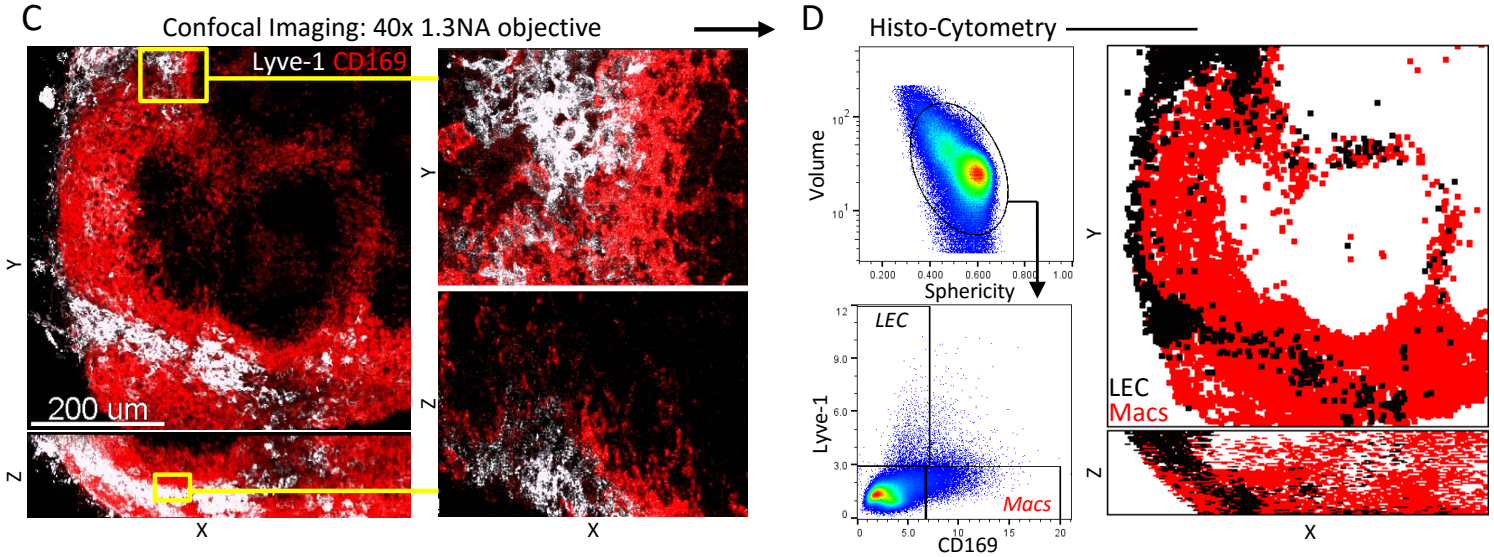


**Figure S7**. $C_e$3D multiplex imaging and high-resolution quantitative Histo-Cytometry.
(A) Same LN as in Main Figure 4A is presented in a rotated orientation, with the individual stains isolated as separate channels. 3D cross-section zoom-in view demonstrates relatively high quality of imaging, but with some spatial overlap between signals from Lyve-1 expressing lymphatic vessels (white) and CD169 expressing medullary macrophages (orange). (B) Cell membrane signals were used to create cell objects and exported for analysis in FlowJo, as presented in Main Figure 4. (C) LN were stained with the CD169 and Lyve-1 antibodies, cleared and imaged with a 40x 1.3NA objective. (D) Images were next segmented with cell statistics exported into FlowJo for (D) quantitative population gating and positional analysis.

# Supplementary Figure 8

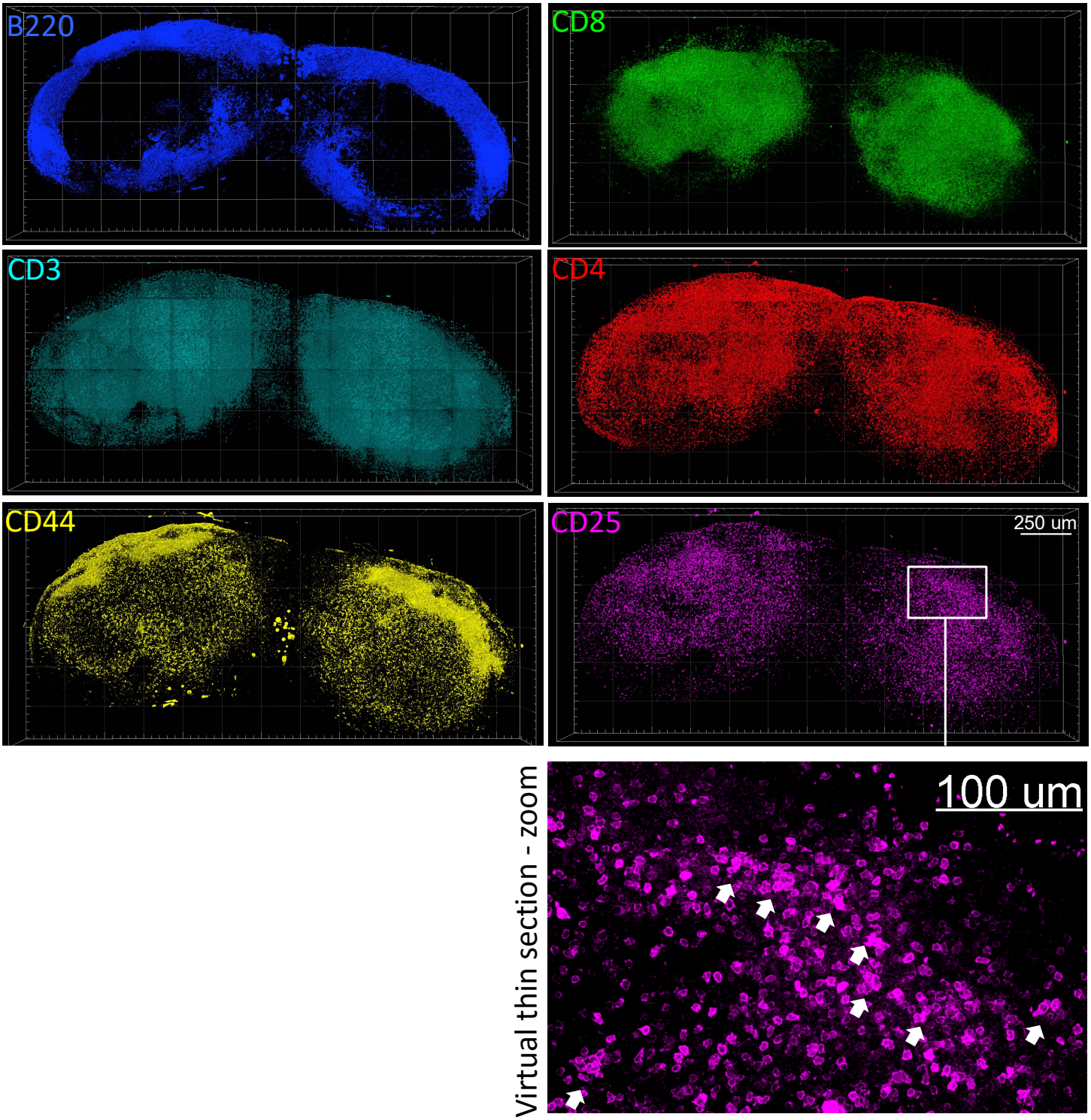


**Figure S8**. Multiplex panel for quantitative $C_e$3D Histo-Cytometry of lymphocyte populations.
Maximum projection images of the individual acquired channels for the merged LN image presented in Main Figure 5A. Zoom-in view of a maximum projection for a 20um-thick virtual slice demonstrates an area enriched in $CD25^+$ cell clusters (arrows).

# Supplementary Figure 9

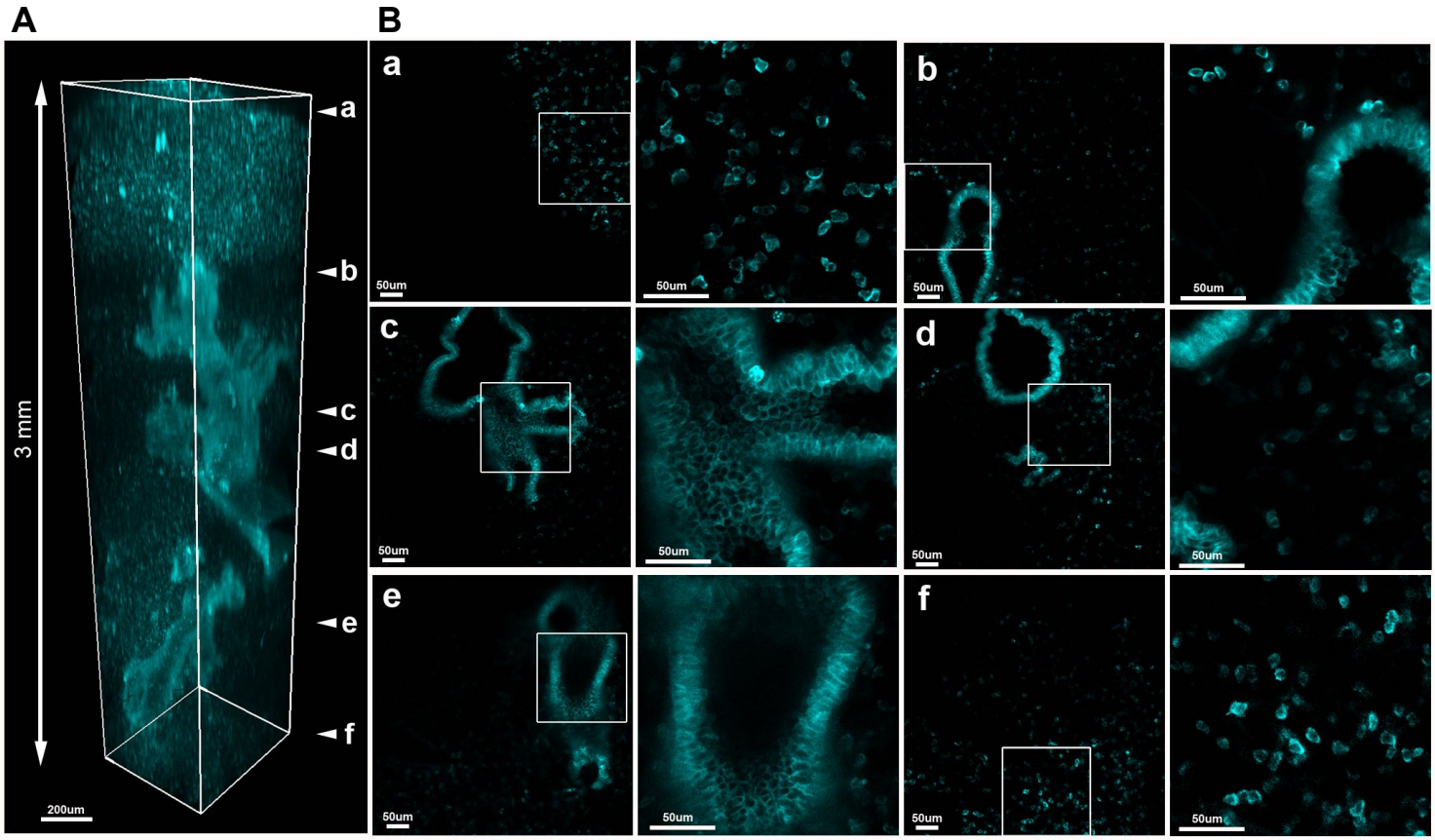


**Figure S9**. High-resolution, large volumetric imaging of $C_e$3D treated tissues.
Lungs were labeled with Alexa 647 conjugated anti-cytokeratin antibody and cleared with $C_e$3D. (A) Tissues were imaged from the anterior to posterior surfaces using the 25x 1.0NA motCORR objective with a step size of 5um and two-photon excitation. Total imaged depth was 3mm. (B) Various virtual optical sections along the imaged volume are presented, with the zoom-in panels demonstrating image quality obtained at the different depths.

# Supplementary Figure 10

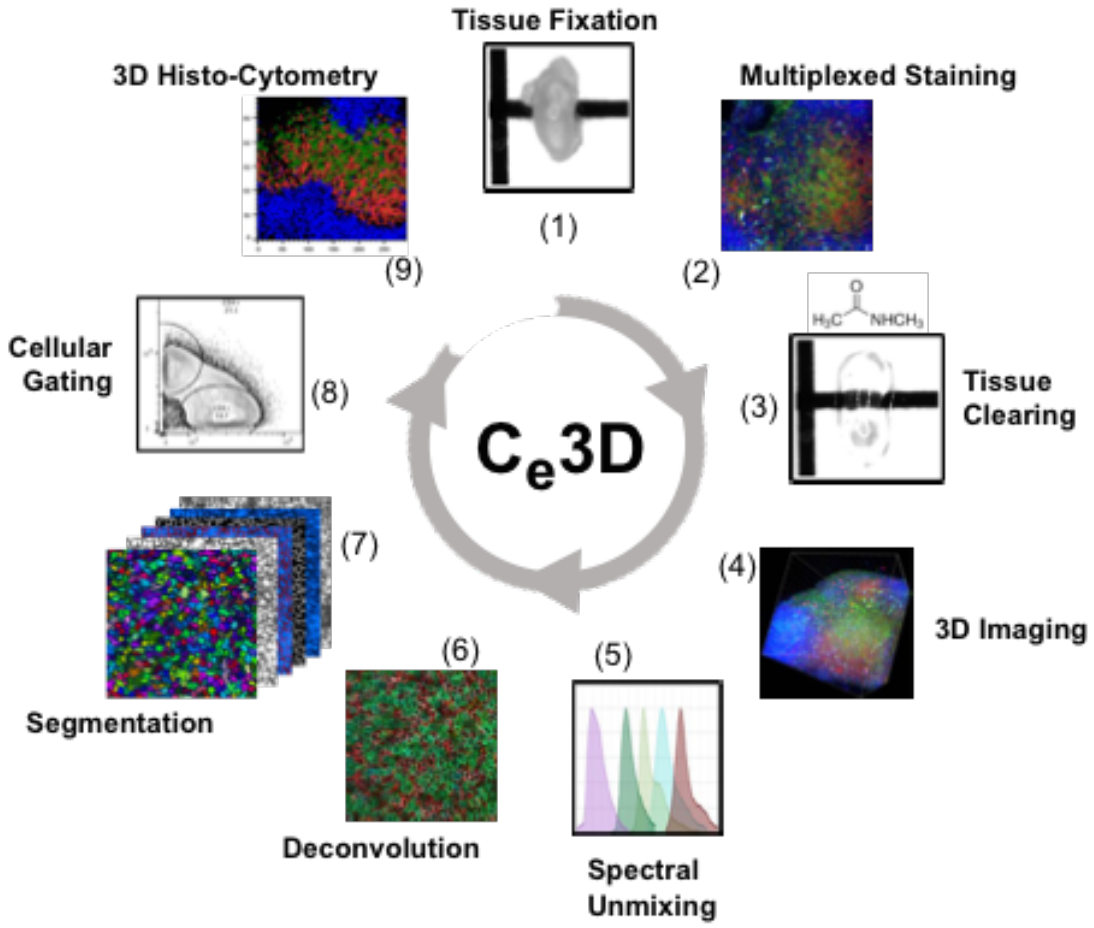


**Figure S10**. $C_e$3D pipeline for tissue clearing, imaging and quantitative Histo-Cytometry. (1) Tissues are fixed, (2) stained with various fluorophore-conjugated antibodies, (3) cleared and (4) imaged. (5) Spectral unmixing to compensate for fluorophore spillover into neighboring detectors is performed. (6) Deconvolution is performed to improve image quality and quantitative accuracy. (7) Images are segmented into individual cell objects, with the objects' statistics then exported into graphing software for (8) population phenotypic gating and (9) quantitative image Histo-Cytometry.

# Table 1

| Method | Transparency | Antibody Staining | Fluorescent Proteins Tested | Fluorophores tested | Antibodies tested | Volume Change | Ease of Use | Clearing Time |
|---|---|---|---|---|---|---|---|---|
| **$C_e$3D** | strong | +++ | GFP, YFP, CFP, DsRED, TdTomato | >25 | 30 | minor shrinkage | +++ | ++ |
| **ScaleS** | strong | + | YFP | ~5 | N/A | no change | - | + |
| **AbScale** | strong | ++ | None | ~5 | <5 | no change | - | + |
| **Scale** | intermediate | - | YFP, DsRed | <5 | <5 | expansion | ++ | + |
| **CUBIC** | strong | +/- | mKate2, mCherry, GFP, YFP | <5 | <5 | expansion | + | ++ |
| **SeeDB** | weak | - | YFP | <5 | <5 | no change | ++ | + |
| **ClearT/T2** | weak | +/- | GFP | <5 | <5 | minor shrinkage | +++ | ++ |
| **CLARITY** | strong | +/- | GFP, YFP, TdTomato | DAPI | 5-10 | expansion | + | + |
| **PACT** | strong | +/- | GFP, YFP | ~5 | 5-10 | expansion | ++ | + |
| **3DISCO** | strong | +++ | GFP, CFP, YFP (rapid quenching) | <5 | <5 | shrinkage | +++ | +++ |
| **iDISCO** | strong | +++ | TdTomato | ~5 | 28 | shrinkage | ++ | +++ |

**Table 1**. Comparison of the various tested tissue-clearing methods with $C_e$3D.
Different parameters desirable for imaging of cleared tissues were compared based on previously published results (P) and empirical observations during direct testing (T).

# Table 2

| Tested Clearing Reagents |
|---|
| **N-Methylacetamide** |
| N-(Hydroxymethyl)acetamide |
| N,N-Diethyl-2-hydroxyacetamide |
| 2-hydroxy-N-Methylacetamide |
| Glycolamide |
| 2-hydroxy-N-Methylacetamide |
| N-Methoxy-N-methylacetamide |
| N-(2-Methoxyphenyl)acetamide |
| N-(Trimethylsilyl)acetamide |
| 2-Chloro-N-(hydroxymethyl)acetamide |
| 2-amino-N,N-dimethylacetamide |
| 2-Methylpentanal |
| Acetamide |
| formamide |
| N-Methylformamide |
| N,N-Dimethylformamide |
| N,N-Dimethylacetamide |
| (±)-3-Amino-1,2-propanediol |
| 3-Methylamino-1,2-propanediol |
| Serinol |
| 3-Methylamino-1-propanol |
| 1-Dimethylamino-2-propanol |
| 3-Dimethylamino-1-propanol |
| Bis(2-hydroxypropyl)amine |
| 2-Dimethylamino-2-methylpropanol |
| Urea |
| Thiourea |
| N-Ethylacetamide |
| N,N'-Dimethylurea |
| 1,1-Dimethylurea |
| 1,3-Diethylurea |
| Tetramethylurea |

**Table 2**. Various reagents tested for overall tissue clarification, conservation of reporter protein fluorescence, preservation of antibody-based staining, overall signal quality and morphological integrity. Main $C_e$3D clearing reagent combined with Histodenz is highlighted in red.

# Table 3

| Tested antibodies compatible with Ce3D | Tested fluorophores compatible with Ce3D |
|---|---|
| B220 (clone RA3-6B2) | CFP |
| CD3 (clone 17A2) | GFP |
| CD4 (clone RM4-5) | YFP |
| CD8 (clone 53-6.7) | tdTomato |
| CD11c (clones N418 and HL3) | DsRed |
| CD25 (clone PC61) | |
| CD44 (clone IM7) | Alexa 405 |
| CD31 (clones 390 and MEC13.3) | Brilliant violet 421 |
| Lyve-1 (clone ALY7) | Pacific Blue |
| EpCam (clone G8.8) | eFluor 450 |
| CD11b (clone M1/70) | BD Horizon V500 |
| MHC-II (clone M5/114.15.2) | Brilliant violet 510 |
| CD169 (clone 3D6.112) | Dylight 405-LS |
| GFAP (clone 2E1.E9) | Alexa 488 |
| CD45 (clone 30-F11) | CF514 |
| CD45.1 (clone A20) | Alexa 546 |
| CD45.2 (clone 104) | Alexa 555 |
| Siglec F (clone 1RNM44N) | Phycoerythrin |
| Tubulin β3 (clones TUJ1 and EP1569Y) | Dylight 521-LS |
| Bcl6 (clone K112-91) | eFluor570 |
| IgD (clone c11-26) | Alexa 594 |
| pStat3 (clone D3A7) | eFluor 615 |
| RORgammaT (clone AFKJS-9) | Alexa 633 |
| Cytokeratin (clone C-11) | CF630 |
| IAV-NP (clone FF750) | Allophycocyanin |
| PD1 (clone 29F.1A12) | Alexa 647 |
| CD35 (clone 8C12) | eFluor 660 |
| ER-TR7 (sc-73355, Santa Cruz) | CF660 |
| Collagen IV (ab19808, Abcam) | Alexa 700 |
| Histone H2B (clone mAbcam 64165) | Alex 750 |
| Nuclear Pore Complex Marker (EnCor Biotech) | |
| KLRG1 (clone 2F1) | DAPI |
| CD301b (clone URA-1) | Hoescht |
| CD207 (clone 929F3.01) | JOJO-1 |
| | CMTMR |
| | CMFDA |

**Table 3**. Tested antibodies (left) and fluorophores (right) that were found compatible with $C_e$3D treated tissues. No incompatible probes were seen among all tested reagents. Large molecular weight (MW) probes that require extended incubation times for tissue penetration, or dyes prone to photobleaching over extended imaging depths are indicated.